universität wien

MASTERARBEIT / MASTER'S THESIS

Titel der Masterarbeit / Title of the Master's Thesis

„Electronic State Unfolding for Plane Waves: an Automatized Computational Implementation."

verfasst von / submitted by

David Dirnberger, BSc

angestrebter akademischer Grad / in partial fulfilment of the requirements for the degree of

Master of Science (MSc)

Wien, 2023 / Vienna, 2023

Studienkennzahl lt. Studienblatt / degree programme code as it appears on the student record sheet:	UA 066 876
Studienrichtung lt. Studienblatt / degree programme as it appears on the student record sheet:	Masterstudium Physics
Betreut von / Supervisor:	Univ.-Prof. Dr.techn. Cesare Franchini

Acknowledgements

I dedicate this thesis to my departed loving father, Manfred. I will always remember how proud he was of my Bachelor thesis although he did not understand everything.
I would like to express my sincere gratitude to my professor Cesare Franchini, who supported me throughout the entire project and assigned me to it in the first place. I am very grateful for all the great opportunities he offered me. My heartfelt gratitude also goes to Michele Reticcioli, who was my supervisor and mentor. Without him the project would not have come so far and I would not have had so many interesting discussions and insights on this topic. The collaboration with him on the paper was inspiring and fun. I also could not have undertaken this journey without the constant support of my family, especially of my grandmother, Magarete, my mother, Gerlinde, my sister and my brother-in-law, Elisa and Tobi, and my uncle, Herbert. Last but not least I would like to thank my flatmates and friends, who always supported me, morally and also financially. A special thanks goes to Annika.

Contents

Abstract

Modern computing facilities enable the application of first-principles density functional theory (DFT) to investigate intricate physical and chemical phenomena. In many cases, these calculations require the use of large supercells to accurately represent the desired properties. However, supercells come with a challenge since they lead to small Brillouin zones in reciprocal space, resulting in folded electronic eigenstates that are difficult to analyse and interpret. To address this issue, various techniques have been proposed to unfold the electronic band structures of supercells into the reciprocal space of an ideal primitive cell. In this context, we introduce an unfolding method directly integrated into the *Vienna Ab initio Simulation Package* (VASP). This approach demands only modest computational resources and offers automated mapping from the supercell's reciprocal space to the Brillouin zone of the primitive cell. Our algorithm, coupled with an integrated post-processing tool called *bands4VASP*, facilitates the computation of effective band structures, Fermi surfaces, and spectral functions.

We will demonstrate the utility of this method by applying it to diverse complex scenarios, focusing on the impact of doping on the band dispersion in the $BaFe_{2(1-x)}Ru_{2x}As_2$ superconductor and the derivation of the effective 3D Fermi surface. Our approach streamlines the analysis of complex physical systems which need huge supercells for an accurate description and enhances our ability to extract meaningful insights from first-principles calculations.

Chapter 1

Introduction

1.1 Density Functional Theory

Density Functional Theory (**DFT**) is a computational quantum mechanical modelling method used to study the electronic structure of molecules and solids and it is the basis of essentially all electronic structure analysis in material science, chemistry and as well other fields. It is based on the idea that the total energy of a system can be expressed as a functional of the electron density $n(\boldsymbol{r})$, rather than the wave function $\Psi(\boldsymbol{r})$, which is for almost all many-electron systems impossible to calculate analytically. The electron density describes the probability of finding an electron at a particular point in space. The Hohenberg-Kohn theorem [1] states that a system of electrons in ground state can be completely described by electron density with all the information about the electronic structure of the system conserved.
Therefore the total energy of a many-electron system can be written as a functional of $n(\boldsymbol{r})$.

$$E[n] = T[n] + E_{ne}[n] + E_{ee}[n] \tag{1.1}$$

Here $T[n]$ is the kinetic energy functional of the electrons, $E_{ne}[n]$ is the energy functional of the coulomb interaction between electrons and nuclei and $E_{ee}[n]$ is the interaction term between electrons and electrons, which can be split into the classical coulomb repulsion or the so called Hartree energy $E_H[n]$ [2] and the exchange-correlation energy $E_{xc}[n]$ which can also take relativistic effects into account. Apparently the exchange-correlation energy is the most difficult part, as it cannot be calculated exactly. Instead, a variety of approximate methods have been developed to calculate this energy term, which will be discussed in more detail later on. Here we already used the Born-Oppenheimer approximation [3], treating the nuclei as fixed with no kinetic energy.

$$E_{KS}[n] = T[n] + E_{ne}[n] + E_H[n] + E_{xc}[n] \tag{1.2}$$

The Kohn-Shame scheme [4] states that the ground state density of the interacting system is equal to some chosen non-interacting auxiliary-system with the following energy functional:

$$E_{aux}[n] = T_s[n] + E_{ne}[n] \tag{1.3}$$

Here the kinetic energy is split into two parts $T[n] = T_s[n] + T_c[n]$, where $T_s[n]$ is the one particle approach for the kinetic energy and the second term $T_c[n]$ is the unknown difference between the single-particle approach and the exact value. This unknown term $T_c[n]$ is shifted to the exchange-correlation energy, to have all unknown quantities in one functional. For the auxiliary-system the determinant approach with one-electron wave functions $\psi_i(\boldsymbol{r})$ sets up the many-body wave function represented by a single Slater-Determinant [5]. The Schrödinger-equation of this N-particle system leads to N of these so called Kohn-Sham equations (KS equations, Eq. 1.4).

$$\left[-\frac{1}{2}\Delta^2 + V_{eff}(\boldsymbol{r})\right]\psi_i(\boldsymbol{r}) = \epsilon_i\psi_i(\boldsymbol{r}) \tag{1.4}$$

Where $V_{eff}(\boldsymbol{r})$ is the effective potential, which is in the non-interacting approach the potential of the nuclei. With these wave functions the density $n(\boldsymbol{r})$ of the auxiliary-system is determined and therefore all other quantities of the non-interacting system.

$$n(\boldsymbol{r}) = \sum_{i=1}^{N} |\psi_i(\boldsymbol{r})|^2 \tag{1.5}$$

$$T_s[n] = -\frac{1}{2}\sum_{i=1}^{N}\int d\boldsymbol{r}\,\langle\psi_i(\boldsymbol{r})|\bigtriangledown^2|\psi_i(\boldsymbol{r})\rangle \tag{1.6}$$

$$E_{ne}[n] = \int V_{eff}(\boldsymbol{r})n(\boldsymbol{r})d\boldsymbol{r} \tag{1.7}$$

With the proposition that the electron density of the auxiliary-system in ground state is the same as in the system of interest in ground state the KS-equations (Eq. 1.4) stay the same, but with a more comprehensive effective potential V_{eff}. Applying the Lagrangian method of undetermined multipliers [6] to the energy functional of the interacting system (Eq. 1.2), yields to the single-particle potential of the interacting approach.

$$V_{eff}(\boldsymbol{r}) = \frac{\delta E_{xc}[n]}{\delta n[\boldsymbol{r}]} + \int d\boldsymbol{r}'\frac{n(\boldsymbol{r}')}{|\boldsymbol{r}-\boldsymbol{r}'|} + V_{ext}(\boldsymbol{r}) \tag{1.8}$$

Where $v_{xc}(\boldsymbol{r}) \equiv \frac{\delta E_{xc}[n]}{\delta n[\boldsymbol{r}]}$ is the exchange-correlation potential and V_{ext} the external potential, which is in most of the cases the induced potential of the nuclei structure. The KS equations (Eq. 1.4) depending on the effective potential V_{eff}, which can be calculated with Eq. 1.8 depending on the electron density $n(\boldsymbol{r})$. This system of equations can solved iteratively with a self-consistent field method. Starting with a guess for the electron density $n(\boldsymbol{r})$, then calculating the effective potential V_{eff} which is used to solve the KS-equations, or a linear combination with the previous potential and the new one. With the new calculated Kohn-Sham orbitals $\psi_i(\boldsymbol{r})$ a improved density (Eq. 1.5) is obtained. This procedure is repeated until a stable solution is found. As it was mentioned

before, the exchange-correlation term is still unsolved. In principle the exchange-correlation $v_{xc}(\boldsymbol{r})$ depends on the electron density $n(\boldsymbol{r})$ of the entire space not only on a specific $\boldsymbol{r}$ and as well some other effects for example the relativistic effects need to take into account for a accurate approach. Obviously some approximation need to be done for a practical usability of this theory. There are a variety of approximate methods, which have been developed to calculate this energy term:

- **L**ocal **D**ensity **A**pproximation (LDA) is the simplest approach. It treats the electron density $n(\boldsymbol{r})$ as the density of a homogeneous electron gas at the position $\boldsymbol{r}$. In general the exchange-correlation energy functional is given by:

$$E_{xc}[n] = \int n(\boldsymbol{r})\epsilon_{xc}(n(\boldsymbol{r}))d\boldsymbol{r} \tag{1.9}$$

  where $\epsilon_{xc}(n(\boldsymbol{r}))$ is the exchange correlation energy per electron of a homogenous electron gas of density $n(\boldsymbol{r})$. However, through the crucial simplification of an uniform electron density, this approximation is very limited and overestimates the strengths of all bonds near equilibrium. For example, LDA calculations for semiconductors are known to yield to band gaps that are $30\% - 50\%$ smaller than what experimental data predicts [8, 7].

- **L**ocal **S**pin **D**ensity Approximation (LSD) additionally considers the difference of electron densities with spin polarisation $n_\uparrow$ and $n_\downarrow$. The functional of the exchange-correlation energy writes as follows [9, 10]:

$$E_{xc}^{LSD}[n_\uparrow, n_\downarrow] = \int d\boldsymbol{r} n(\boldsymbol{r})\epsilon_{xc}(\boldsymbol{r}_s, \xi) \tag{1.10}$$

  where $n(\boldsymbol{r}) = n_\uparrow + n_\downarrow$, $\xi = (n_\uparrow - n_\downarrow)/n$ and r_s is the local Seitz radius.

$$r_s = \left(\frac{3}{4\pi n}\right)^{\frac{1}{3}} \tag{1.11}$$

  The LSD Approximation constitutes an improvement to the LDA, due to the more detailed assumptions, but still underestimates the binding energy of the core electrons and overestimates it for atoms in a molecule or solid [9].

- **G**eneralized **G**radient **A**pproximation (GGA) is a more sophisticated method. Instead of only considering the density $n(\boldsymbol{r})$, GGA is also taking the gradient $\nabla n(\boldsymbol{r})$ into account [9, 10, 11] . The exchange-correlation energy functional is therefore given as follows:

$$E_{xc}^{GGA}[n_\uparrow, n_\downarrow] = \int d\boldsymbol{r} n(\boldsymbol{r}) f(n_\uparrow, n_\downarrow, \nabla n_\uparrow, \nabla n_\downarrow) \tag{1.12}$$

  The choice of $f(n_\uparrow, n_\downarrow, \nabla n_\uparrow, \nabla n_\downarrow)$ depends on the physical system and is still studied. In comparison with the local functionals above, the "semilocal" GGA improves total energies [9],energy barriers and structural energy differences [12] and atomization energies [9, 13].

Nowadays mostly a modified mix of these functionals are used for DFT calculations. In this work all DFT calculations were done with *VASP* [14] and the PE (PBE) functional [15, 10].

Overall, DFT has become an indispensable tool in modern theoretical chemistry and material science, as it provides a powerful and efficient way to study the electronic structure of complex systems. While the method has its limitations, it has proven to be a highly accurate and reliable approach for a wide range of applications.

1.2 Bloch-Theorem

The Bloch-Theorem gives a general solution to an one particle Schrödinger equation for a periodic potential, in this case an one electron Schrödinger equation. This is used for band structure analysis and the unfolding method. To get there, we consider the static Schrödinger equation (Eq. 1.13) with an one electron hamiltonian in a periodic potential $V(\boldsymbol{r}) = V(\boldsymbol{r}+\boldsymbol{R})$, where $\boldsymbol{R} = n_1\boldsymbol{a}_1+n_2\boldsymbol{a}_2+n_3\boldsymbol{a}_3$ is an arbitrary translation vector of the Bravais lattice with $n_i \in \mathbb{Z}$ and the primitive cell vectors $\boldsymbol{a_1}$, $\boldsymbol{a_2}$ and $\boldsymbol{a_3}$.

$$\mathcal{H}\Psi(\boldsymbol{r}) = E\Psi(\boldsymbol{r}) \qquad \mathcal{H} = -\frac{\hbar^2}{2m}\Delta^2 + V(\boldsymbol{r}) \tag{1.13}$$

The periodic potential $V(\boldsymbol{r})$ can be developed in a Fourier series (Eq. 1.14).

$$V(\boldsymbol{r}) = \sum_{\boldsymbol{G}} V_{\boldsymbol{G}} e^{i\cdot\boldsymbol{G}\cdot\boldsymbol{r}} \tag{1.14}$$

Where $\boldsymbol{G} = h\boldsymbol{b}_1 + k\boldsymbol{b}_2 + l\boldsymbol{b}_3$ is a reciprocal lattice vector. The Bloch-Theorem states that the general ansatz for the wave function is a linear combination of plane waves.

$$\Psi(\boldsymbol{r}) = \sum_{\boldsymbol{k}} C_{\boldsymbol{k}} e^{i\boldsymbol{k}\cdot\boldsymbol{r}} \tag{1.15}$$

This results can now plugged in to the Schrödinger equation (Eq. 1.13).

$$\sum_{\boldsymbol{k}} \frac{\hbar^2 k^2}{2m} C_k e^{i\boldsymbol{k}\cdot\boldsymbol{r}} + \sum_{\boldsymbol{k},\boldsymbol{G}} C_{\boldsymbol{k}} V_{\boldsymbol{G}} e^{i(\boldsymbol{k}+\boldsymbol{G})\cdot\boldsymbol{r}} = E \sum_{\boldsymbol{k}} C_{\boldsymbol{k}} e^{i\boldsymbol{k}\cdot\boldsymbol{r}} \tag{1.16}$$

Finally we can rename the summation indices $\boldsymbol{k} \to \boldsymbol{k} - \boldsymbol{G}$ in the second term of Eq. 1.16 and recap it.

$$\sum_{\boldsymbol{k}} e^{i\boldsymbol{k}\cdot\boldsymbol{r}} \left[\left(\frac{\hbar^2 k^2}{2m} - E \right) C_{\boldsymbol{k}} + \sum_{\boldsymbol{G}} V_{\boldsymbol{G}} C_{\boldsymbol{k}-\boldsymbol{G}} \right] = 0 \tag{1.17}$$

This equation has to be satisfied for every $\boldsymbol{r}$, which means that every summand from the sum of $\boldsymbol{k}$ has to be zero. Which leads us to a representation of the Schrödinger equation in the reciprocal space (Eq. 1.18).

$$\left(\frac{\hbar^2 k^2}{2m} - E\right) C_{\boldsymbol{k}} + \sum_{\boldsymbol{G}} V_{\boldsymbol{G}} C_{\boldsymbol{k}-\boldsymbol{G}} = 0 \tag{1.18}$$

As stated in Eq. 1.18, every $\boldsymbol{k}$ is related to a set of coefficients $(C_{\boldsymbol{k}}, C_{\boldsymbol{k}-\boldsymbol{G}}, C_{\boldsymbol{k}-\boldsymbol{G}'}, C_{\boldsymbol{k}-\boldsymbol{G}''}, ...)$, which only differs in a reciprocal lattice vector $\boldsymbol{G}$. The decoupling of the Schrödinger equations, allows us to write every one electron wave function $\Psi_{\boldsymbol{k}}$ as a sum of wave vectors over the reciprocal lattice vectors $\boldsymbol{G}$.

$$\Psi_{\boldsymbol{k}}(\boldsymbol{r}) = \sum_{\boldsymbol{G}} C_{\boldsymbol{k}-\boldsymbol{G}} e^{i(\boldsymbol{k}-\boldsymbol{G})\cdot\boldsymbol{r}} \tag{1.19}$$

We can rewrite this result to highlight the structure of the solution.

$$\Psi_{\boldsymbol{k}}(\boldsymbol{r}) = \left(\sum_{\boldsymbol{G}} C_{\boldsymbol{k}-\boldsymbol{G}} e^{-i\boldsymbol{G}\cdot\boldsymbol{r}}\right) e^{i\boldsymbol{k}\cdot\boldsymbol{r}} \tag{1.20}$$

The solution of the one electron Schrödinger equation for a periodic potential is the product of a plane wave and a lattice periodic modular function $u_{\boldsymbol{k}}(\boldsymbol{r}) = u_{\boldsymbol{k}}(\boldsymbol{r} + \boldsymbol{R})$. The principle is shown for a one dimensional case in Figure 1.1.

$$\Psi_{\boldsymbol{k}}(\boldsymbol{r}) = u_{\boldsymbol{k}}(\boldsymbol{r}) e^{i\boldsymbol{k}\cdot\boldsymbol{r}} \tag{1.21}$$

Function in Eq. 1.21 is called Bloch function with periodicity $\Psi_{\boldsymbol{k}}(\boldsymbol{r}) = \Psi_{\boldsymbol{k}+\boldsymbol{G}}(\boldsymbol{r})$. To every $\boldsymbol{k}$-vector and Bloch function $\Psi_{\boldsymbol{k}}$ belongs an infinite set of energy eigenvalues $E_n(\boldsymbol{k}) = E(\boldsymbol{k}+\boldsymbol{G}_n)$. The index n is used to assign the energy eigenvalue E_n to the associated reciprocal lattice vector $\boldsymbol{G}_n$ and is called band index [16, 17].

1.3 Fermi level, Fermi energy and Fermi surface

The **Fermi level** refers to the total of kinetic and potential energy of a thermodynamic system at any temperature and even for complex interacting systems. In metals it is the energy of the highest occupied single particle state at absolute zero temperature. The **Fermi energy** is the energy difference between the highest and the lowest occupied single-particle state in a quantum system of non-interacting fermions at absolute zero temperature. In metals it is the energy difference between Fermi level and the lowest occupied single-particle state [19, 18].

In band theory the energy eigenstates of the electrons in a solid are so close together that they are considered as a semi-continuous accumulation of states or the so called bands. There are bands crossing Fermi level and at absolute zero this would imply a separation of occupied states (below Fermi) and unoccupied states (above Fermi) as it is shown in panel **a** in Figure 1.2. This enables the electrons to absorb an amount of energy ΔE and occupy the state with that additional energy, but it should be noted that the electrons are not able to change to a state which is already occupied,

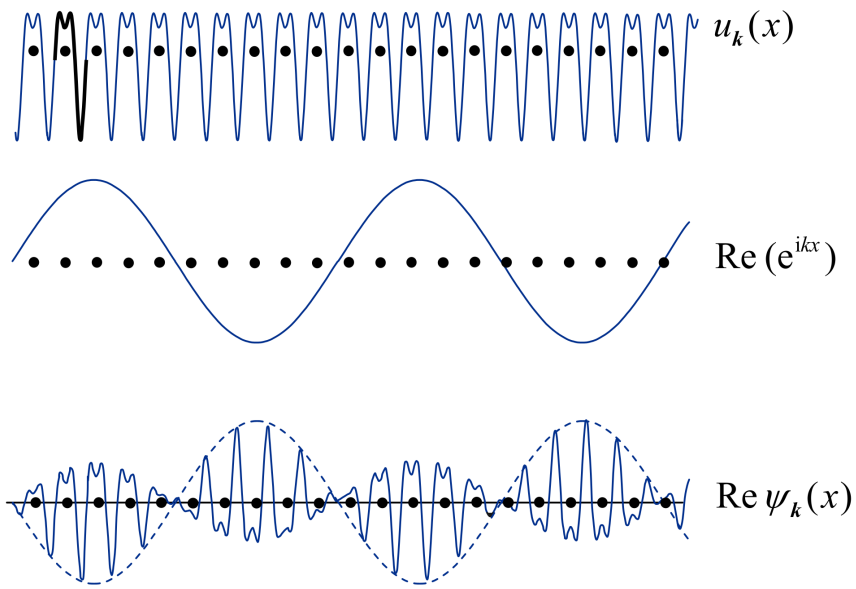

Figure 1.1: One dimensional showcase of a Bloch function. The lattice periodic function $u_k(x)$ describes the potential caused by the nucleus, which are illustrated by the black dots. The real part of the phase e^{ikx} is representing the plane wave. The combination of both (Eq. 1.21) is visualized by the real part of the Bloch function $\Psi_{\boldsymbol{k}}$ [17].

because of the Pauli exclusion principle [18]. In terms of band theory is this the mechanics behind electric conduction.

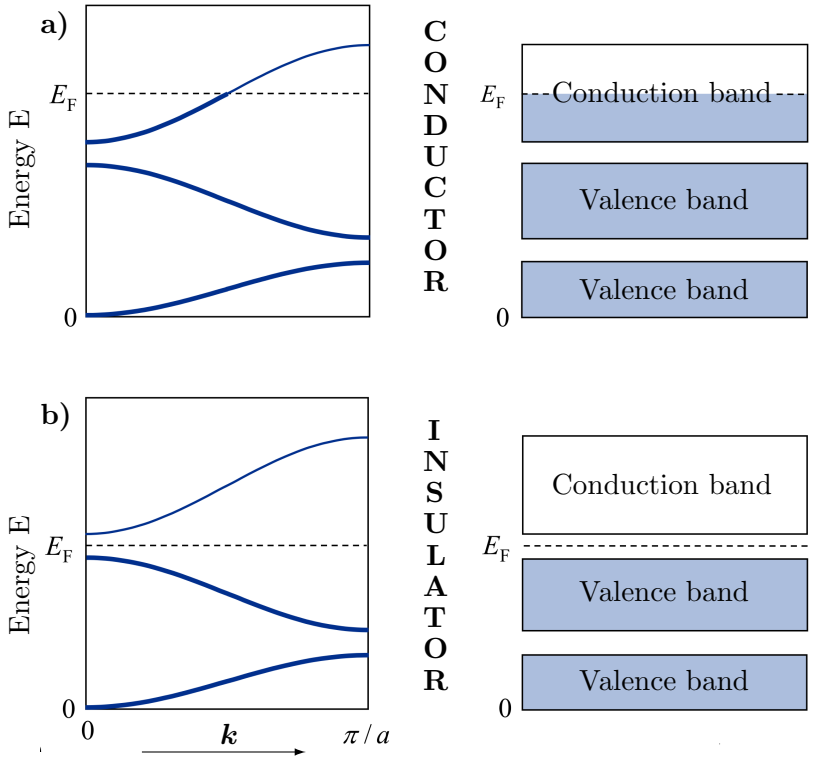

Figure 1.2: Depiction of a band structure with Fermi level E_F. Panel **a)** demonstrates the situation, where the conduction band is crossing at Fermi $E(\boldsymbol{k}) = E_F$ with half filled states, which implies that the solid associated with this band structure is a conductor. In panel **b)** all states of the valence bands are completely occupied, but there are no occupied states in the conduction band. For a large enough energy gap this is associated with an insulator. Adapted from [17].

In conclusion, a solid with crossing bands at Fermi level is either a metal (conductor) or a semimetal. If there is a gap around the Fermi level, the electrons need at least absorb the energy difference ΔE_{gap} of the highest occupied state to the lowest unoccupied one. Depending on the value of ΔE_{gap} the solid is either an insulator or a semiconductor.

By outlining the states with constant energy $E(\boldsymbol{k}) = E_F$ in the Brillouin zone according to their $\boldsymbol{k}$-vector we obtain an isosurface of energy E_F, the so called **Fermi surface**. Such a surface in the reciprocal space shows all occupied states at Fermi level E_F. It can either be a cut through the Brillouin zone, which we will call 2D Fermi surface, or a hypersurface with all the states $E(\boldsymbol{k}) = E_F$ highlighted in the Brillouin zone which we call 3D Fermi surface. The shape, geometry and topology of the Fermi surface give significant information about the conducting properties of the material, these studies are called fermiology. A quantitative description can be found in the Appendix A.

1.4 Unfolding Method

The goal of the unfolding method is to obtain the energy dispersion relation or the so called band structure for large supercells, projected onto a smaller primitive cell. The band structure related with the supercell $E(\boldsymbol{K})$, can be very hard to interpret and analyse due to the vast amount of information. An example of band structure obtained from a primitive cell versus the more complex band structure from a supercell of the same compound is shown in Figure 1.3. Therefore the unfolding scheme unfolds the band structure, obtained in the smaller reciprocal space of the supercell, onto the larger reciprocal space of the primitive cell and projects the supercell eigenstates $|\boldsymbol{K}\rangle$ onto the primitive cell eigenstates $|\boldsymbol{k}\rangle$. The resulting band structure $E(\boldsymbol{k})$ is called effective band structure (EBS).

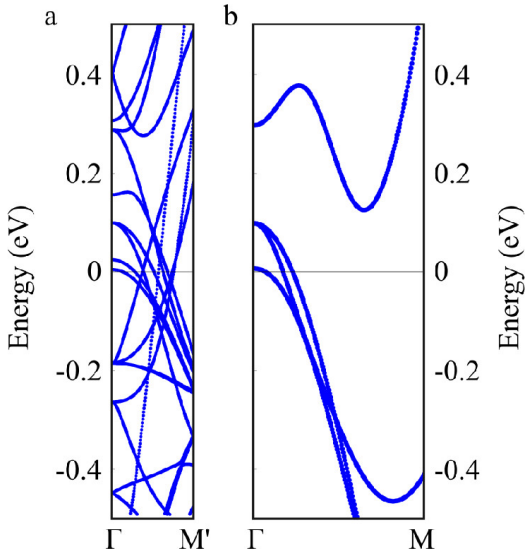

Figure 1.3: Example of eigenstate folding for the pristine $BaFe_2As_2$ compound. Band structures obtained by using (a) a two times larger supercell and (b) a primitive cell [20].

1.4.1 Folded space

The **primitive cell** (PC) is the smallest possible unit cell and always corresponds to a single lattice point. It is defined by a lattice $\hat{a}_{ij} = (\vec{a}_i)_j$ or in reciprocal space $\hat{b}_{ij} = (\vec{b}_i)_j$. As shown in Section 1.2 we can write the eigenstates as a plane wave expansion (Eq. 1.21), but for further considerations we rewrite the function in Eq. 1.20 in Dirac notation as the eigenvectors $|\boldsymbol{k}n\rangle$ of the primitive cell and label them with $n \in \mathbb{N}$, the band index.

$$|\boldsymbol{k}n\rangle = \left[\sum_{\boldsymbol{g}} B_{\boldsymbol{k}n}(\boldsymbol{g}) e^{i\boldsymbol{g}\cdot\boldsymbol{r}}\right] e^{i\boldsymbol{k}\cdot\boldsymbol{r}} \tag{1.22}$$

A **supercell** (SC) is also defined by a lattice $\hat{A}_{ij} := (\vec{A}_i)_j$ or in reciprocal space $\hat{B}_{ij} := (\vec{B}_i)_j$, but has no limitation for lattice point. It is often used in *ab initio* calculations as unit cell to model complex systems with broken symmetry. The Brillouin zone of the SC (SBZ) is in general smaller than the Brillouin zone of the PC (pbz), that is the reason why the energy bands obtained from

SBZ are folded and have to be unfold in the *pbz*. The eigenvectors $|\boldsymbol{K}m\rangle$ of the SC can be expressed as follows.

$$|\boldsymbol{K}m\rangle = \left[\sum_{\boldsymbol{G}} C_{\boldsymbol{K}m}(\boldsymbol{G}) e^{i\boldsymbol{G}\cdot\boldsymbol{r}}\right] e^{i\boldsymbol{K}\cdot\boldsymbol{r}} \tag{1.23}$$

The connection between SC and PC is given by a transformation matrix $\hat{M}$

$$\hat{A} = \hat{M}\hat{a} \quad \text{and} \quad det(\hat{M}) \neq 0 \quad \text{where} \quad m_{ij} \in \mathbb{Z} \tag{1.24}$$

This means the SC has to be an integer spacial multiple of the PC. For every parallelepiped, which is formed from the linear independent lattice of both the SC and the PC, the volume is given by the absolute value of the determinant from the lattice matrix.

$$vol(SC) = |det(\hat{A})| = |det(\hat{M}\hat{a})| = |det(\hat{M})| \cdot |det(\hat{a})| = |det(\hat{M})| \cdot vol(PC)$$

$$\Rightarrow \quad |det(\hat{M})| = \frac{vol(SC)}{vol(PC)} \tag{1.25}$$

Because most of our considerations and calculations taking part in the reciprocal space, we need to derive the relation between *SBZ* and *pbz*. Therefore we start with the definition of reciprocal lattice for SC and PC, respectively.

$$\begin{aligned} \hat{b}\hat{a}^T = 2\pi\mathbb{1} \quad &\Leftrightarrow \quad \hat{b} = 2\pi(\hat{a}^{-1})^T \\ \hat{B}\hat{A}^T = 2\pi\mathbb{1} \quad &\Leftrightarrow \quad \hat{B} = 2\pi(\hat{A}^{-1})^T \end{aligned} \tag{1.26}$$

$$\hat{B} = 2\pi(\hat{A}^{-1})^T = 2\pi[(\hat{M}\hat{a})^{-1}]^T = 2\pi(\hat{M}^{-1})^T(\hat{a}^{-1})^T = (\hat{M}^{-1})^T\hat{b}$$

$$\Rightarrow \quad \hat{B} = (\hat{M}^{-1})^T\hat{b} = \tilde{M}\hat{b} \tag{1.27}$$

Where $\tilde{M} = (\hat{M}^{-1})^T$ is the transformation matrix of the reciprocal lattice. If we finally take a look at the ratio of the volumes in reciprocal space, the *pbz* is larger than the *SBZ*. This can be shown using the same scheme as in Eq. 1.25, leading to the following ratio.

$$|det(\hat{M})| = \frac{vol(pbz)}{vol(SBZ)} \tag{1.28}$$

In the theoretical part we are talking about the eigenvectors or eigenstates $|\boldsymbol{k}n\rangle$ (Eq. 1.22) and $|\boldsymbol{K}m\rangle$ (Eq. 1.23) of *pbz* and *SBZ*, respectively. In the practical part of this work the focus lies more on $\boldsymbol{k}$-points, which are 3-dimensional real vectors $\boldsymbol{k} \in \mathbb{R}^3$ used as sampling points in the Brillouin zone. In the expression of eigenvectors $|\boldsymbol{k}n\rangle$ and $|\boldsymbol{K}m\rangle$ they are the "wave vector" of the plane wave modulation $e^{i\boldsymbol{k}\cdot\boldsymbol{r}}$. A $\boldsymbol{k}$-point refers to a set of eigenvectors $|\boldsymbol{k}n\rangle$, which means that this is a

surjective relation in Hilbert space $|\boldsymbol{k}n\rangle : \mathbb{R}^3 \twoheadrightarrow \mathbb{C}$ and therefore no unique identification.

Knowing that, we want to derive the relation between a $\boldsymbol{k}$-point of *pbz* $\boldsymbol{k}_b$ and a $\boldsymbol{k}$-point of *SBZ* $\boldsymbol{K}_B$. The basis vectors $\vec{b}_i$ and $\vec{B}_i$ are stored in rows in the lattice matrices, therefore the lattice matrix needs to be transposed for a basis transition into Cartesian coordinates $\boldsymbol{K}_C$.

$$\boldsymbol{K}_C = \hat{B}^T \boldsymbol{K}_B \quad \text{and} \quad \boldsymbol{K}_C = \hat{b}^T \boldsymbol{k}_b \tag{1.29}$$

Using the inverse transition for *SBZ*:

$$\begin{aligned} \boldsymbol{K}_B &= (\hat{B}^T)^{-1} \boldsymbol{K}_C \\ &= (\hat{B}^T)^{-1} \hat{b}^T \boldsymbol{k}_b \end{aligned} \tag{1.30}$$

Now plugging in Eq. 1.27:

$$\begin{aligned} \boldsymbol{K}_B &= [(\tilde{M}\hat{b})^T]^{-1} \hat{b}^T \boldsymbol{k}_b \\ &= (\hat{b}^T \tilde{M}^T)^{-1} \hat{b}^T \boldsymbol{k}_b \\ &= (\tilde{M}^T)^{-1} (\hat{b}^T)^{-1} \hat{b}^T \boldsymbol{k}_b \\ \\ \Rightarrow \quad \boldsymbol{K}_B &= \hat{M} \boldsymbol{k}_b \\ \boldsymbol{k}_b &= \hat{M}^{-1} \boldsymbol{K}_B \end{aligned} \tag{1.31}$$

These $\boldsymbol{k}$-point transition from *SBZ* to *pbz* and vice versa are implemented in VASP, which we will go into more detail later on.

1.4.2 Projection Scheme

The previous results states that a vector $\boldsymbol{K}$ in *SBZ* unfolds exactly onto $det(\hat{M})$ vectors $\boldsymbol{k}_i$, where always a reciprocal vector $\boldsymbol{G}_i$ in *SBZ* exists as the connection between the two spaces.

$$\boldsymbol{k}_i = \boldsymbol{K} + \boldsymbol{G}_i \qquad i = 1, ..., det(\hat{M}) \tag{1.32}$$

There is as well the lowercase $\boldsymbol{g}$ associated with the reciprocal lattice vector of the larger *pbz* and knowing, that $\{\boldsymbol{g}_i\} \subset \{\boldsymbol{G}_i\}$ means that there is always a reciprocal vector ΔG so we can express the vectors $\boldsymbol{G}$ as:

$$\boldsymbol{G} = \boldsymbol{g} + \boldsymbol{G}_\Delta \tag{1.33}$$

One advantage of the unfolding method is that the two crystal systems *SBZ* and *pbz* do not have to be the same. The two cells have to be a spacial integer multiple of each other, but the atomic structure of the *SC* don't has to fullfil the periodicity from the *pc*. These, in general, different local environments disrupts the orthogonality for the eigenstates of each crystal system. Therefore we define the spectral weight for any $\boldsymbol{K}$ and its associated $\boldsymbol{k}_i$.

$$P_{\boldsymbol{K}_m}(\boldsymbol{k}_i) = \sum_n |\langle \boldsymbol{K}m|\boldsymbol{k}_i n\rangle|^2 \tag{1.34}$$

This so called Bloch character represents the probability to unfold the state $|\boldsymbol{K}m\rangle$ of *SBZ* onto the quantum number $\boldsymbol{k}_i$ of *pbz*. The eigenvectors of *pbz* building a complete orthogonal set, but not necessary an orthonormal one. Starting with the definition of an orthonormal basis of vectors.

$$\langle \boldsymbol{k}n|\boldsymbol{k}m\rangle = \delta_{nm} \tag{1.35}$$

For these two eigenvectors, the L^2 inner-product looks like:

$$\langle \boldsymbol{k}n|\boldsymbol{k}m\rangle = \sum_{\boldsymbol{g},\boldsymbol{g}'} B^*_{\boldsymbol{k}n}(\boldsymbol{g}) B_{\boldsymbol{k}m}(\boldsymbol{g}') \int d^3r e^{i(\boldsymbol{g}-\boldsymbol{g}')\boldsymbol{r}} \tag{1.36}$$

This integral is non-zero if $\boldsymbol{g} = \boldsymbol{g}'$ and equals the volume V of the crystal system.

$$\Rightarrow \quad \langle \boldsymbol{k}n|\boldsymbol{k}m\rangle = V \sum_{\boldsymbol{g}} B^*_{\boldsymbol{k}n}(\boldsymbol{g}) B_{\boldsymbol{k}m}(\boldsymbol{g}) \tag{1.37}$$

With Eq. 1.35 we write the orthonormal eigenvectors:

$$|\boldsymbol{k}n\rangle = \frac{1}{\sqrt{V}} \left[\sum_{\boldsymbol{g}} B_{\boldsymbol{k}n}(\boldsymbol{g}) e^{i\boldsymbol{g}\cdot\boldsymbol{r}}\right] e^{i\boldsymbol{k}\cdot\boldsymbol{r}} \tag{1.38}$$

For reasons of simplification we let the normalisation factor $\frac{1}{\sqrt{V}}$ be part of the coefficients $B_{\boldsymbol{k}n}$, since they are not determined yet. As we seen in Section 1.2 the eigenvectors $|\boldsymbol{k}n\rangle$ build a complete basis of all periodic functions with the plane-wave modulation $e^{i\boldsymbol{k}\boldsymbol{r}}$, which is just an additional phase shift. This group of functions building an isomorphism with the group of plane-waves $e^{i\boldsymbol{g}\boldsymbol{r}}$ from the reciprocal lattice vectors $\boldsymbol{g}$. That means that the dimensions are equal $\Rightarrow \quad dim(n) = dim(\boldsymbol{g})$, which allows us to rewrite the coefficients as a quadratic matrix $\tilde{B}$.

$$\tilde{B}_{\boldsymbol{g}n}(\boldsymbol{k}) := B_{\boldsymbol{k}n}(\boldsymbol{g}) \tag{1.39}$$

If we combine the results with Eq. 1.35 and Eq. 1.37 in matrix notation, we see that the coefficient matrix $\tilde{B}$ is unitary.

$$\tilde{B}^\dagger \cdot \tilde{B} = \mathbb{1} \quad \Leftrightarrow \quad \tilde{B} \cdot \tilde{B}^\dagger = \mathbb{1} \tag{1.40}$$

To evaluate the inner-product of the definition from Bloch character (Eq. 1.34), we need to rewrite the eigenvector $|\boldsymbol{K}m\rangle$ from the *SBZ* and express the reciprocal lattice vector $\boldsymbol{G}$ in terms of the lattice vector $\boldsymbol{g}$ from *pbz* (Eq. 1.33).

$$\begin{aligned} |\boldsymbol{K}m\rangle &= \left[\sum_{\boldsymbol{G}} C_{\boldsymbol{K}m}(\boldsymbol{G}) e^{i\boldsymbol{G}\cdot\boldsymbol{r}}\right] e^{i\boldsymbol{K}\cdot\boldsymbol{r}} \\ &= \sum_{\boldsymbol{G}_\Delta} e^{i\boldsymbol{G}_\Delta\cdot\boldsymbol{r}} \left[\sum_{\boldsymbol{g}} C_{\boldsymbol{K}m}(\boldsymbol{g}+\boldsymbol{G}_\Delta) e^{i\boldsymbol{g}\cdot\boldsymbol{r}}\right] e^{i\boldsymbol{K}\cdot\boldsymbol{r}} \end{aligned} \tag{1.41}$$

The inner product of *pbz* and *SBZ* eigenvectors yields to:

$$\langle \boldsymbol{k}n|\boldsymbol{K}m\rangle = \sum_{\boldsymbol{G}_\Delta}\sum_{\boldsymbol{g},\boldsymbol{g}'} B^*_{\boldsymbol{k}n}(\boldsymbol{g})C_{\boldsymbol{K}m}(\boldsymbol{g}+\boldsymbol{G}_\Delta)\int e^{i[\boldsymbol{G}_\Delta-(\boldsymbol{k}-\boldsymbol{K})]\boldsymbol{r}}\; e^{i(\boldsymbol{g}-\boldsymbol{g}')\boldsymbol{r}}\; d^3r \tag{1.42}$$

This integral is non-zero if $\boldsymbol{g}=\boldsymbol{g}'$ and when $\boldsymbol{K}$ unfolds into $\boldsymbol{k}$ through $\boldsymbol{G}_\Delta$, which is the case for $\boldsymbol{G}_\Delta = \boldsymbol{k}-\boldsymbol{K}$.

$$\langle \boldsymbol{k}n|\boldsymbol{K}m\rangle = \sum_{\boldsymbol{g}} B^*_{\boldsymbol{k}n}(\boldsymbol{g})C_{\boldsymbol{K}m}(\boldsymbol{g}+\boldsymbol{k}-\boldsymbol{K}) \tag{1.43}$$

Using the last equation and its conjugated form and plugging into Eq. 1.34, we get:

$$P_{\boldsymbol{K}m}(\boldsymbol{k}_i) = \sum_n \left[\sum_{\boldsymbol{g},\boldsymbol{g}'} B_{\boldsymbol{k}n}(\boldsymbol{g}')B^*_{\boldsymbol{k}n}(\boldsymbol{g})C_{\boldsymbol{K}m}(\boldsymbol{g}+\boldsymbol{k}_i-\boldsymbol{K})C^*_{\boldsymbol{K}m}(\boldsymbol{g}'+\boldsymbol{k}_i-\boldsymbol{K})\right] \tag{1.44}$$

With the result from Eq. 1.40 the expression simplifies to:

$$\boxed{P_{\boldsymbol{K}m}(\boldsymbol{k}_i) = \sum_{\boldsymbol{g}} |C_{\boldsymbol{K}m}(\boldsymbol{g}+\boldsymbol{k}_i-\boldsymbol{K})|^2} \tag{1.45}$$

In that expression for Bloch character $P_{\boldsymbol{K}m}(\boldsymbol{k}_i)$, the necessary information from PC are solely geometrical from the connection of the reciprocal lattice vector $\boldsymbol{g}$ to the vectors $\boldsymbol{k}_i$. In comparison to the definition of Bloch character (Eq. 1.34) this approach offers the benefit of circumventing any computations related to the primitive cell and sidesteps the need for direct comparisons between the two spaces, which might cause technical difficulties and could lead into a much higher calculation effort[21, 22, 20]. This will be revisited in Chapter 2 *Methodology, Development and Application*, where the unfolding implementation in VASP is explained. Finally we can define the spectral function for the continuous energy spectrum:

$$A(\boldsymbol{k}_i, E) = \sum_m P_{\boldsymbol{K}m}(\boldsymbol{k}_i)\delta(E_m - E) \tag{1.46}$$

1.4.3 Effective Band Structure (EBS)

The band theory uses Bloch's theorem (Sec. 1.2) to solve the one electron Schrödinger equation (Eq. 1.13). The obtained energy eigenvalues $E_n(\boldsymbol{k})$ form a dispersion relation, which is called band structure. In the unfolding theory there are 2 different spaces which are relevant, *SBZ* and *pbz*. Starting from the dispersion relation $E_n(\boldsymbol{K})$ of *SBZ* the Bloch character (Eq. 1.34) states for each eigenvector $|\boldsymbol{K}m\rangle$ and a related one of the primitive cell $|\boldsymbol{k}_i n\rangle$ a probability $P_{\boldsymbol{K}m}(\boldsymbol{k}_i)$. That weighted energy eigenvalues $E(\boldsymbol{k})$ of the primitive cell, obtained from the dispersion relation $E(\boldsymbol{K})$ of the supercell is called effective band structure (EBS). In the case that the supercell is a mere spacial repetition of the primitive cell, it represents the same physical material. The band structure $E(\boldsymbol{K})$ of SC is in that case just the folded band structure of PC $E(\boldsymbol{k}) \Rightarrow \quad \langle \boldsymbol{k}_i n|\boldsymbol{K}m\rangle = \delta_{nm}$. This

is shown in Figure 1.4, where an effective band structure, obtained from a two times larger super cell, is compared with the band structure from the primitive cell. The energy bands from super cell are as expected twice as much as the bands from primitive cell band structure. The Bloch character identifies the folded bands not related to the primitive cell with $P_{\boldsymbol{K}m} = 0$, which is shown with a grey colour. That means if we truncate all states with $P_{\boldsymbol{K}m} = 0$ we get the same band structure as from the PC calculation. The benefit of this method lies obviously not in applying it to a mere spacial repetition of a PC, rather in applying it to a different atomic structure, which breaks the translation symmetry.

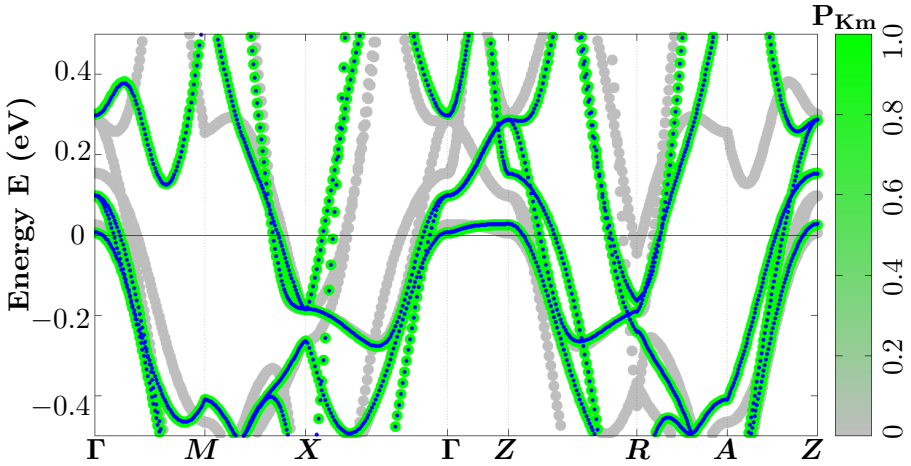

Figure 1.4: Effective band structure of pure $BaFe_2As_2$ (blue) with a super cell two times as large as the primitive cell which is represented with a grey-to-green colour gradient band structure [20].

In that case only the eigenstates of the SC $|\boldsymbol{K}m\rangle$ are still quantum quantities, because they fulfil the translation symmetry of the whole system. Eigenstates of PC $|\boldsymbol{k}_i n\rangle$ break this symmetry and therefore they can't be interpreted as quantum quantities any more. The contribution of a specific $|\boldsymbol{k}_i n\rangle$ state to a $|\boldsymbol{K}m\rangle$ eigenstate takes in these cases the values between 0 and 1.

$$0 \leq \langle \boldsymbol{k}_i n | \boldsymbol{K}m \rangle \leq 1 \tag{1.47}$$

In such a case the Bloch character is an important indicator to identify the relevant bands. Examples of effective band structures with broken translation symmetries are shown in Figure 2.5 and 2.9. Figure 2.5, panels a and b, show the importance of Bloch character as an indicator. In a) are all states visible, whereas in b) only the relevant states with a Bloch character larger than 0.025 are shown.

Chapter 2

Methodology, Development and Application

In this chapter we are focusing on 3 parts of the project, the numerical implementation of the eigenstate unfolding scheme in VASP, the post-processing tool bands4VASP and the analysis of the testcase $BaFe_{2(1-x)}Ru_{2x}As_2$. These parts are based on each other in that order, therefore we will go into detail for every part and discuss the methodology, development and applications, respectively. Because one of the aims of the project was a "user-friendly" interface, some of these methods are explained in this chapter as well. A more detailed description of the usage of this software can be found on the documentation sites, respectively [14, 23]. The quintessence of the project was published in *The Journal of Physical Chemistry C* under the title *Electronic State Unfolding for Plane Waves: Energy Bands, Fermi Surfaces, and Spectral Functions* [20].

2.1 Unfolding algorithm embedded in VASP

The first project is a user-friendly and memory efficient implementation of the unfolding scheme in VASP [14, 20]. Starting from a given SC in the POSCAR file, there are basically 2 different ways of defining an unfolding calculation. Recalling the relation for the connection of SC and PC:

$$\hat{A} = \hat{M}\hat{a} \quad and \quad \hat{B} = (\hat{M}^{-1})^T\hat{b} \tag{2.1}$$

We can either define the primitive cell $\hat{a}$ in real space or $\hat{b}$ in reciprocal space, or we define the transformation matrix $\hat{M}$, which is called INTMUL in the INCAR file. If ionic informations are given in POSCAR.prim, they are used to reduce the number of k-points due to symmetry, which can reduce the extensiveness of the calculation, but don't influence the result of the calculation. There is also the possibility that the lattice in the POSCAR file is no spacial repetition of the lattice given in POSCAR.prim, within a precision of $\sim 10^{-7}$. The super cell has to be a spacial multiple of the primitive cell, as it is stated in Eq. 1.24, therefore the algorithm takes the closest

cell in size and shape to the given one, which satisfies relation in Eq. 2.1 according to the super cell, assumes it as the new primitive cell and writes this lattice in CONTCAR.prim. It will also write the calculated primitive cell in POSCAR.prim, if the transformation matrix $\hat{M}$ is given.
The next step is to determine both sets of $\boldsymbol{k}$-points $\{\boldsymbol{k}\}, \{\boldsymbol{K}\}$ in the irreducible part of the Brillouin zone, in which one of these sets is given. In the KPOINTS file one has the option to determine the $\boldsymbol{k}$-points sampling either in the *pbz* or *SBZ*. This feature is a great advantage due to calculation costs and needs to be explained in more detail.
The default unfolding calculation takes the given set of $j \times \boldsymbol{k}$-points $\{\boldsymbol{K}\}$ from *SBZ* and calculates the Bloch character (Eq. 1.45) of all pairs $\boldsymbol{K} \leftarrow \boldsymbol{k}_i - \boldsymbol{G}$, which is for j given $\boldsymbol{K}$-points and $det(\hat{M}) \times \boldsymbol{k}_i$ vectors for one $\boldsymbol{K}$-point (Eq. 1.32) an amount of $N_d = j \cdot det(\hat{M})$ separately calculated Bloch characters.

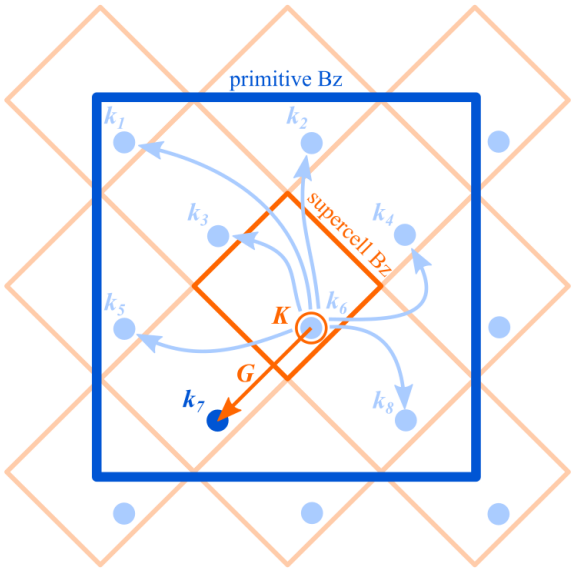

Figure 2.1: Illustration of the folding scheme in a two-dimensional $2\sqrt{2} \times 2\sqrt{2}$ super cell. The primitive cell's Brillouin Zone *pbz* is depicted by a large blue square, while *SBZ* is represented by smaller orange squares. The arrows symbolize the transformation of eigenstates originating from $|\hat{M}_{2\sqrt{2}\times 2\sqrt{2}}| = 8$ distinct $\boldsymbol{k}_i$-vectors (PC) (represented as filled circles) into a single $\boldsymbol{K}$-vector (SC) (depicted as an open orange circle). Additionally, the reciprocal lattice vector $\boldsymbol{G}$ highlights the eigenstates unfolding from the $\boldsymbol{K}$-vector back to a specific $\boldsymbol{k}_i$-vector [20].

In most cases of unfolding calculations one is only interested in the effective band structure, which refers to the primitive cell. So the other possibility is to define directly the $\boldsymbol{k}$-points in the primitive cells *pbz* and calculate only the Bloch character for one unique $\boldsymbol{K}$-point connected through a specific combination of the reciprocal lattice vectors with the given $\boldsymbol{k}$-point of the primitive cell $\boldsymbol{K} \leftarrow \boldsymbol{k}_i - \{\boldsymbol{G}\}$, which is outlined in Figure 2.1 for a two-dimensional $2\sqrt{2} \times 2\sqrt{2}$ supercell. Nevertheless VASP determines all the quantities like Bloch- or orbital characters in terms of the SC, that's why we used relation in Eq. 1.31 to bijectively transform the $\boldsymbol{k}$-points of *pbz* in terms of *SBZ*. For j given $\boldsymbol{k}$-points the total amount of calculated Bloch characters is simply $N_c = j$. In

comparison with the default case we get a ration of $\frac{N_d}{N_c} = det(\hat{M})$, which means that the new way of defining the $\boldsymbol{k}$-points is saving $j \cdot (det(\hat{M}) - 1)$ Bloch character calculations.

2.2 The post-processing tool bands4VASP

The post-processing tool *bands4VASP* [23] was build to calculate the Fermi vectors from the EBS, organise and visualise it as well as some additionally features like an automated calculation of the 2D Fermi surface and a setup routine for preparing the 2D Fermi surface calculations with VASP. Figure 2.5 b) demonstrate the first procedure, which is a filtering of the eigenstates regarding to the Bloch character and breaks it down to the physical relevant eigenstates. The challenge lies more in developing an algorithm which is able to detect the roots from the effective band structure, respective to the Fermi level. For a primitive cell band structure it could just follow the band index to identify every eigenstate from one energy band and writing an algorithm calculating the roots is just straight forward. For unfolded bands, however, the band index stays not any more the same for the whole band. Only segments of the band belong to the same band index. Mostly there are a lot of eigenstates close together with similar properties, which complicates the whole situation even more. One strategy would be to collect and merge the similar states and represent them as one averaged state. During the process of developing and testing, it was getting more clear that every available quantity needs to take into account. But these values are sensitive to the physical system, that's why the decision was to use an input file (*INPAR*) with adjustable default values. All the properties needed for distinguish the states are listed in the Appendix B.

The algorithm goes through the eigenstates for every $\boldsymbol{k}$-point, respectively. A specific state (n, m) of k-point $\boldsymbol{k}_n$ and band index m has an energy eigenvalue of E_{nm}. The algorithm picks all states in between the energy interval $[E_{nm} - EDIF; E_{nm} + EDIF]$, which has an orbital character difference to state (n, m) less than **ODISTINCT** and compress all collected eigenstates to a weighted averaged state (Eq. 2.2). Let $\{E_n\}_{m=1,\dots,d}$ be a set of energy eigenstates found around E_{n1}, where E_{n1} is part of the set it self. Let's define as well a simplified expression of the Bloch character (Eq. 1.34) $P_{nm} := P_{\boldsymbol{K}m}(\boldsymbol{k}_n)$. The weighted averaged energy of the band centre of mass writes as:

$$\tilde{E}_n = \frac{\sum_m P_{nm} \cdot E_{nm}}{\sum_m P_{nm}} \tag{2.2}$$

Depending on the options **BAVERAGE** and **OAVERAGE** the orbital- and Bloch characters are either summed up or they are weighted with the following relations:

$$\tilde{P}_n = \frac{\sum_m P_{nm}(\Delta E_n - \mid \tilde{E}_n - E_{nm} \mid)}{\sum_m (\Delta E_n - \mid \tilde{E}_n - E_{nm} \mid)} \tag{2.3}$$

$$\tilde{Oc}_n^{\theta} = \frac{\sum_m Oc_{nm}^{\theta}(\Delta E_n - \mid \tilde{E}_n - E_{nm} \mid)}{\sum_m (\Delta E_n - \mid \tilde{E}_n - E_{nm} \mid)} \tag{2.4}$$

$$\Delta E_n = max(\{E_n\}_m) - min(\{E_n\}_m) \tag{2.5}$$

Here ΔE_n is the maximal energy interval of all the energy states which will be compressed to one band center of mass and Oc^{θ}_{nm} is the orbital character of orbital $\theta = s, py, px, pz, dxy, ...$, band index m and $\boldsymbol{k}$-point n. These compression of the eigenstates is schematically shown in Sketch 2.2 a).

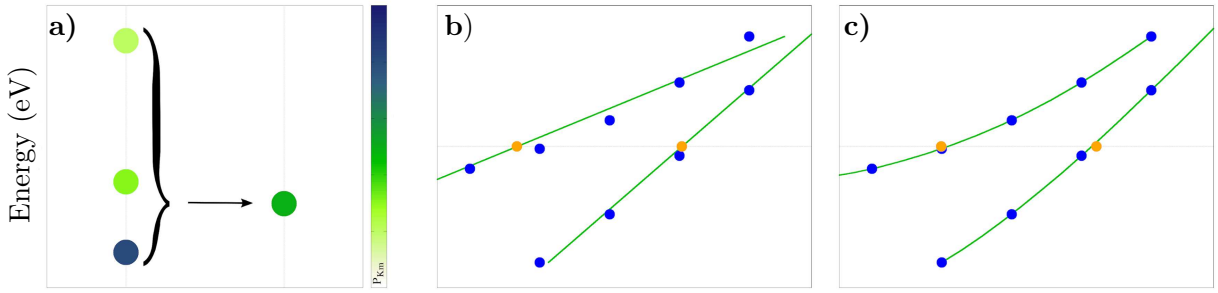

Figure 2.2: Panel a) depicts the weighted averaging method (Eq. 2.2) for the scattered Energy eigenstates obtained from unfolding. b) and c) Show two different samples which represents two bands with a more linear local behaviour and one with a more sinuous geometry. Panel b) demonstrates the roots calculation with linear regression. Panel c) shows the polynomial interpolation, which can be performed analytically for a polynomial of degree $n-1$, because of the low number of points $n < 10$. This method has especially an advantage for sinuous bands around Fermi, but the results can differ in general more than the ones from linear regression.

The processed data with the weighted states will be considered as normal states, to not unnecessary overcomplicate the explanations. With these processed band structure bands4VASP goes through it again and scans for Fermi roots, or the so called Fermi vectors. If a pair of states crossing Fermi is found, some quantities needs to be checked:

- The difference of the energy of two states needs to be less than **EGAP**.
- The difference of the Bloch character needs to be less than **DBLOCH**.
- The difference of the orbital character needs to be less than **ODISTINCT**.

Once these criteria are fulfilled, **NPOINTS** above and below Fermi are determined for finally calculating the Fermi vectors. This works almost as before, despite it checks additionally the gradient condition, set with **GRADIENTD**. As it is sketched in Fig. B the difference of two proximate energy eigenvalues from the same effective band are taken to linearly estimate the energy value of the next state E_{prox}. The **GRADIENTD** factor multiplied with **EGAP** defines the energy interval around the estimated value for which the energy value at the proximate $\boldsymbol{k}$-point has to be in $[E_{prox} - EGAP \cdot GRADIENTD; E_{prox} + EGAP \cdot GRADIENTD]$. For a local linear behaviour of the band **GRADIENTD** should be set to a low value, where **EGAP** represents the slope.

Once it founds all desired states of the effective band, the intersection point is either calculated with linear regression or with polynomial interpolation. Calculating the roots with the straight-line from linear regression is straight forward, but for the polynomial interpolation there are a lot of different methods to approximate the intersection with Fermi. We chose the *Regula falsi* method. Both ways of calculating the roots are sketched in Fig. 2.2.

The other properties of the Fermi vector can be obtained by using the same average method as before (Eqs. 2.3,2.4). These calculated Fermi roots are transformed to a 3-dimensional Fermi vector and written in the *FERMIROOTS.dat* file. In the case that no Fermi roots were found, bands4VASP calculates the energy gap around the Fermi level. This is done by taking the difference from the value of the lowest energy eigenstate above Fermi and the highest energy eigenstate below it.

It must be noted that, since we are taking the average twice from the original data, it is very important that we only consider a few states $N \leq 10$ for this whole procedure. For a suitable $\boldsymbol{k}$-point density, this procedure will only take states very close to Fermi into account, which gives a quite accurate estimation. In Section 2.5 we will do a qualitative discussion with our testcase and compare the results obtained with this method with experimental data.

Additionally we implemented in bands4VASP an automatic determination of the 2D Fermi surface, if results are available in the required structure. If Fermi surface mode is activated it will first figure out the orthonormal basis vectors of the surface, where the calculations were done. The basis set is used for the transformation of Fermi vectors into terms of the surface. If symmetry points are defined in the input file, it reflects all Fermi vectors according to the symmetry. At the end all data are written in the file *Fermisurface.dat* and as well the data of the Fermi surface spectral function in the file *Fermisurface.specfun.dat*.

For a more detailed and practical description of all the parameters and functionalities, see the documentation of bands4VASP [23].

2.3 Testcase $BaFe_{2(1-x)}Ru_{2x}As_2$

At first we want to introduce our testcase $BaFe_{2(1-x)}Ru_{2x}As_2$, which we were using for some benchmark and as well to show some applications of the new implementation and the unfolding scheme in general. The pnictide $BaFe_{2(1-x)}Ru_{2x}As_2$ is a perfect candidate for testing the unfolding method. On one side the metal-to-superconductor transition caused by Ru doping is one of the situation, where the unfolding scheme can unveil its capabilities. On the other side $BaFe_{2(1-x)}Ru_{2x}As_2$ is a well known pnictide and there exists many theoretical and experimental data that we used as reference to test our own implementation [24]-[25].

The pnictide $BaFe_2As_2$ crystallizes in a Body-centred tetragonal structure with a I4/mmm space group. The conventional $\hat{\boldsymbol{A}}$ and the primitive lattice $\hat{\boldsymbol{a}}$ is given by the lattice vectors:

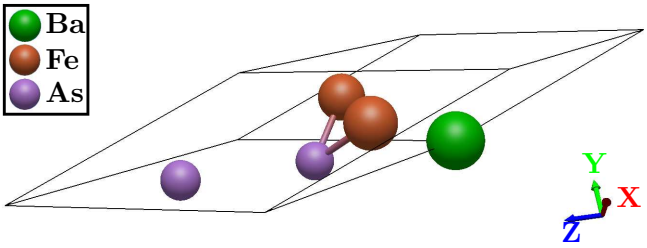

Figure 2.3: The BTC primitive cell of $BaFe_2As_2$. The perspective was chosen to have a good view on the location of all atoms.

$$\begin{aligned} \boldsymbol{A}_1 &= (a,0,0) & \boldsymbol{a}_1 &= (-\frac{a}{2},\frac{a}{2},\frac{c}{2}) \\ \boldsymbol{A}_2 &= (0,a,0) & \boldsymbol{a}_2 &= (\frac{a}{2},-\frac{a}{2},\frac{c}{2}) \\ \boldsymbol{A}_3 &= (0,0,c) & \boldsymbol{a}_3 &= (\frac{a}{2},\frac{a}{2},-\frac{c}{2}) \end{aligned}$$

Where $a = 3.9600\ \mathring{A}$, $c = 13.0100\ \mathring{A}$ are the lattice constants for the pure ($x = 0$) $BaFe_2As_2$ compound and $a = 4.0063\ \mathring{A}$, $c = 12.8254\ \mathring{A}$ for the 25% Ru-doped and relaxed compound $BaFe_{1.5}Ru_{0.5}As_2$. The atomic positions of all 5 components in the primitive cell in terms of the lattice vectors are given by [26]:

$$\begin{aligned} &\boldsymbol{Ba}\ (0,0,0) \\ &\boldsymbol{Fe}\ (0.75,0.25,0.5) \\ &\boldsymbol{Fe}\ (0.25,0.75,0.5) \\ &\boldsymbol{As}\ (0.35,0.35,0) \\ &\boldsymbol{As}\ (0.65,0.65,0) \end{aligned}$$

The primitive cell and the position of the atoms in it, are visualized in Figure 2.3. With all the important data of the primitive cell we can define the super cells by using the transformation matrices $\hat{M}_2, \hat{M}_8, \hat{M}_{16}$ with Eq. 1.24.

$$\hat{M}_2 = \begin{pmatrix} 0 & 1 & 1 \\ 1 & 0 & 1 \\ 1 & 1 & 0 \end{pmatrix}, \quad \hat{M}_8 = \begin{pmatrix} 0 & 2 & 2 \\ 2 & 0 & 2 \\ 1 & 1 & 0 \end{pmatrix}, \quad \hat{M}_{16} = \begin{pmatrix} 0 & 4 & 4 \\ 2 & 0 & 2 \\ 1 & 1 & 0 \end{pmatrix}$$

The spacial ratio of primitive cell to super cell is given by Eq. 1.28 with $det(\hat{M})$ which results in a $2, 8$ and 16 times bigger super cell than the primitive cell, with a maximum number of 80 atoms for the M_{16} system. We visualized the M_2 cell to show the structure of the super cell and compared it with the Ru doped case (Fig. 2.4). The tests and benchmark with the doped case were done with a Ru concentration of 25% or $BaFe_{1.5}Ru_{0.5}As_2$.

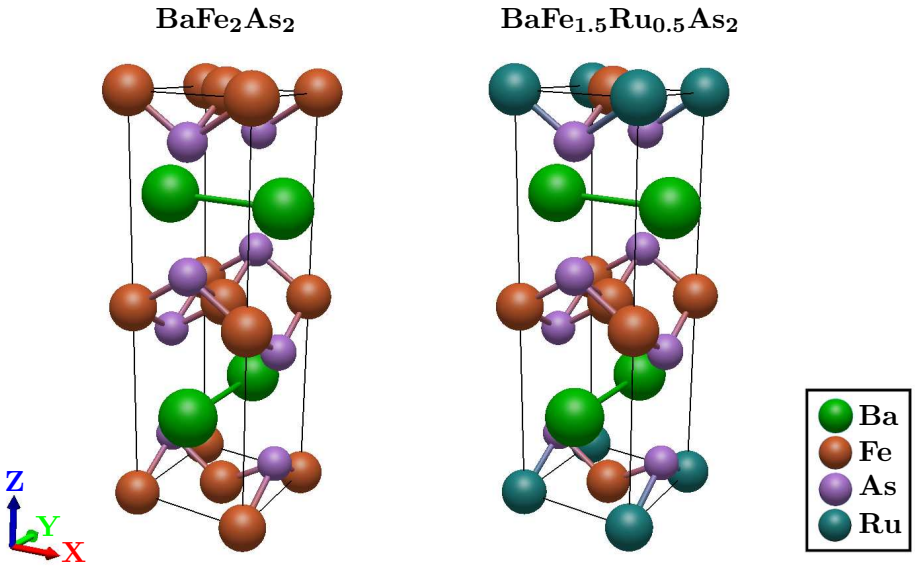

Figure 2.4: Two super cells set up with $\hat{M}_2$ from $BaFe_2As_2$. On the left side is the two times larger pure super cell and on the right hand side the 25% Ru doped $BaFe_{1.5}Ru_{0.5}As_2$ cell. The atoms were placed at all lattice points in the cell.

2.4 Benchmark and Testing

The first step for verifying the new implementation was to test the trivial case, where the super cell is a pure spacial repetition of the primitive cell. To do so, we chose the super cell set up with M_2, as it is shown in Figure 2.4. This testcase was already mentioned in Section 1.4.3 and the results are shown in Figure 1.4. As expected all the Bloch character of the folded band structure were either 1 or 0 and nothing between. If we only colour the energy values with $P_{\boldsymbol{K}m}(\boldsymbol{k}_i) = 1$, we get the same band structure as it is obtained from the primitive cell.

The next step of the Benchmark and testing phase was to calculate EBS for the doped case and compare it with the published results [27, 28]. The calculated EBS with the new implementation are shown in Figure 2.5 and matches with the already published results. We used this experiment to test the post-processing tool **bands4VASP**, which originated as well from this project.

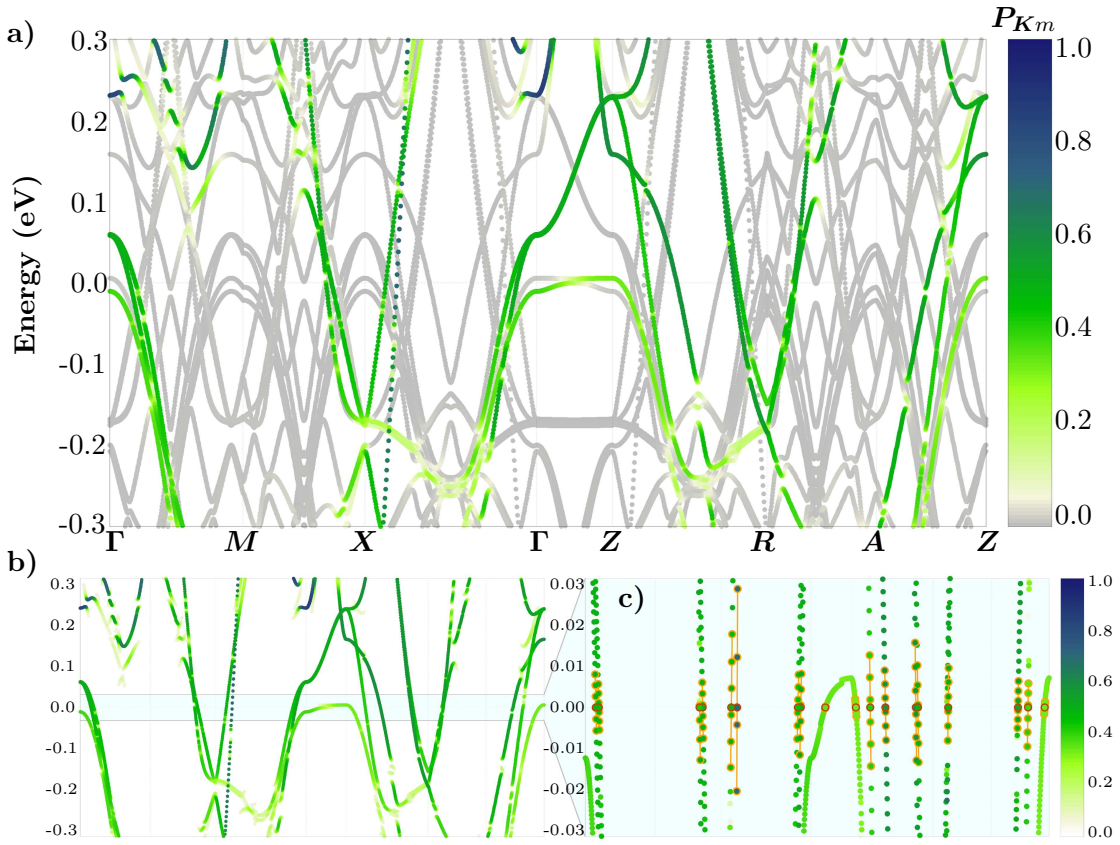

Figure 2.5: Three effective band structure plots for the pnictide $BaFe_{1.5}Ru_{0.5}As_2$ with a 8 times larger super cell (M_8) along high symmetry points of the first Brillouin zone. The Bloch character of the eigenstates is indicated with the gradient colour palette from gray (white) to blue. Panel a) shows the unfiltered plot with all folded eigenstates. Panel b) the same as panel a), but eigenstates with a Bloch character less than the threshold of 0.025 are truncated. Panel c) shows the processed version of the EBS with the automatic calculated Fermi vectors.

Knowing that the implementation reproduced the results for the simple case as expected, we moved our attention to performance tests. The idea was to use 3 different super cells which we introduced in Section 2.3 and as well a varying number of $\boldsymbol{k}$-points $\{150, 200, 300\}$. An unfolding calculation in VASP is doing much more than the calculation of Bloch characters and energy eigenvalues, even setting up everything for unfolding is taking huge calculation capacity. That is the reason why we decided to do as well a reference calculation, with the same setup but unfolding deactivated. The three setups are:

$\boldsymbol{u_0}$ memory usage without unfolding.

$\boldsymbol{u_{old}}$ the old unfolding method.

$\boldsymbol{u_{new}}$ the improved method with chosen $\boldsymbol{k}$-points.

The calculation were all done along the $\boldsymbol{\Gamma}$-$\boldsymbol{M}$ path with the pnictide $BaFe_{1.5}Ru_{0.5}As_2$ on the *Vienna Scientific Cluster 3*[29]. The ratio of the efficiency of the new and the old implementation was calculated with the following relation and arranged in Table 2.1:

$$100 \cdot \left[1 - \frac{(u_{new} - u_0)}{(u_{old} - u_0)}\right] \ [\%] \tag{2.6}$$

# $\boldsymbol{k}$-points	**150**	**200**	**300**
$det(M) = 2$	41.6%	54.3%	69.1%
$det(M) = 8$	70.2%	77.9%	85.9%
$det(M) = 16$	79.7%	86.5%	*

Table 2.1: Benchmark of the new unfolding implementation in VASP. This table shows reference calculations for different super cell sizes M_2, M_8 and M_{16}, as well different amount of $\boldsymbol{k}$-points with the testcase $BaFe_{1.5}Ru_{0.5}As_2$. The calculations were done on the *Vienna Scientific Cluster 3*[29]. The setup with the * was only possible to calculate with the new algorithm.

We used as well some other setups to test our implementation. The pristine rutile $TiO_2(110)$ with reduced dimensionality was an interesting candidate for the unfolding scheme, because super cells are practical to simulate the creation of surface oxygen vacancies, which in turn result in the stabilization of small electron polarons. These electron polarons correspond to electrons that become highly localized on titanium ions and are coupled to the phonon field. We discovered at the in-gap bands that two polaronic states are not degenerated, which is a phenomenon attributed to their interaction with the CO molecules. The more detailed description of this examination as well as the other exertion with a noncollinear magnetic ordering system of $EuCd_2As_2$ is written in the articles [20, 30].

2.5 The effective Fermi surface

The Fermi surface is an important instrument for analysing conducing phenomena in crystals and therefore we want to extend this concept with an effective Fermi surface. The Fermi surface is derived from the energy dispersion relation $E(\boldsymbol{k})$ of the system and it represents all states of constant energy $E(\boldsymbol{k}) = E_F$ in the Brillouin zone (Sec. 1.3). From the unfolding scheme we obtain the effective band structure (Sec. 1.4.3) and as a result Fermi vectors, which are representing as well states of constant energy $E(\boldsymbol{k}) = E_F$ in the Brillouin zone. In that picture we define the effective Fermi surface coming from unfolding calculation with every depicted eigenstate associated with a Bloch character $0 \leq P_{\boldsymbol{K}m}(\boldsymbol{k}_i) \leq 1$. We applied this concept to our testcase $BaFe_{1.5}Ru_{0.5}As_2$ and used as an orientation the basal $\boldsymbol{\Gamma}$-plane spectral Fermi surfaces with different Ru concentrations $x = \{0, 0.25, 0.5, 0.75\}$ (Fig. 2.6 i) as well as the 3D Fermi surfaces of $BaFe_2As_2$ (Fig. 2.6 ii) and $BaRu_2As_2$ (Fig. 2.6 iii).

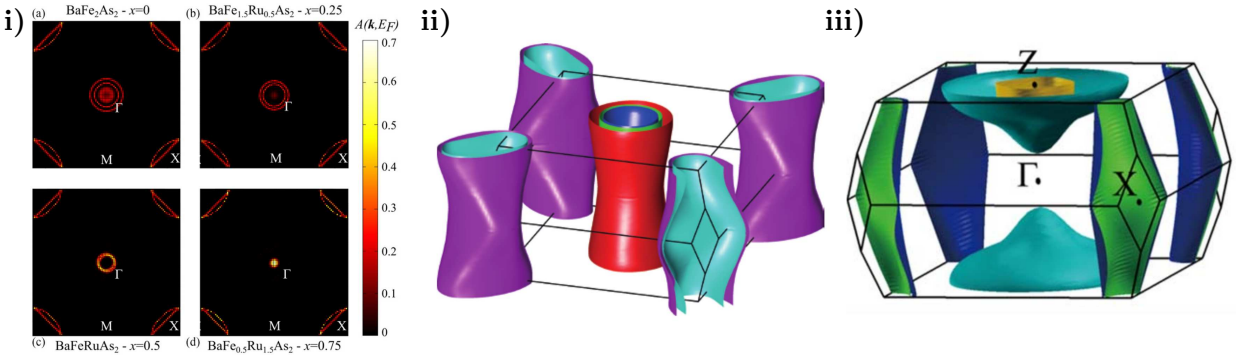

Figure 2.6: **i)** Four basal $\boldsymbol{\Gamma}$-plane Fermi surfaces with different Ru concentration $x = \{0, 0.25, 0.5, 0.75\}$ for the pnictide $BaFe_{2(1-x)}Ru_{2x}As_2$ obtained from spectral function [28]. **ii)**) 3D Fermi surface of $BaFe_2As_2$ in the first Brillouin zone [31]. **iii)** 3D Fermi surface of $BaRu_2As_2$ in the first Brillouin zone [32].

The space group of the Body-centred tetragonal system of 25% Ru-doped Ba-122 is as well the $I4/mmm$ space group, which means that we only have to calculate $\frac{1}{4}$ for the 2D effective Fermi surfaces and $\frac{1}{8}$ for the 3D one and utilize the symmetry. To calculate the 3D effective Fermi surface we partitioned the $\frac{1}{8}$ of the Brillouin zone with 8 equidistant parallel slices, starting from the basal $\boldsymbol{\Gamma}$-plane up to the $\boldsymbol{Z}$-plane. From the 3D Fermi surfaces of $BaFe_2As_2$ and $BaRu_2As_2$ we expected a similar structure with a cylindrical like geometry centred in the middle and at the 4 edges of the Brillouin zone. Because the $\boldsymbol{k}$-point sampling need to be in line for the unfolding with post-processing, the choice of the sampling is crucial for the quality of the resulting surface, as we demonstrated it in Figure 2.9 in the right inset. Therefore we set up a radial sampling centred at $\boldsymbol{\Gamma}$ and one at $\boldsymbol{X}$.

From the results we extracted $8 \times 2D$ effective Fermi surfaces with bands4VASP. Three of these Fermi surfaces obtained from the spectral function (Eq. 1.46) are shown below in Figure 2.7 and the unprocessed Fermi vectors in the Brillouin zone are shown in Figure 2.8 a).

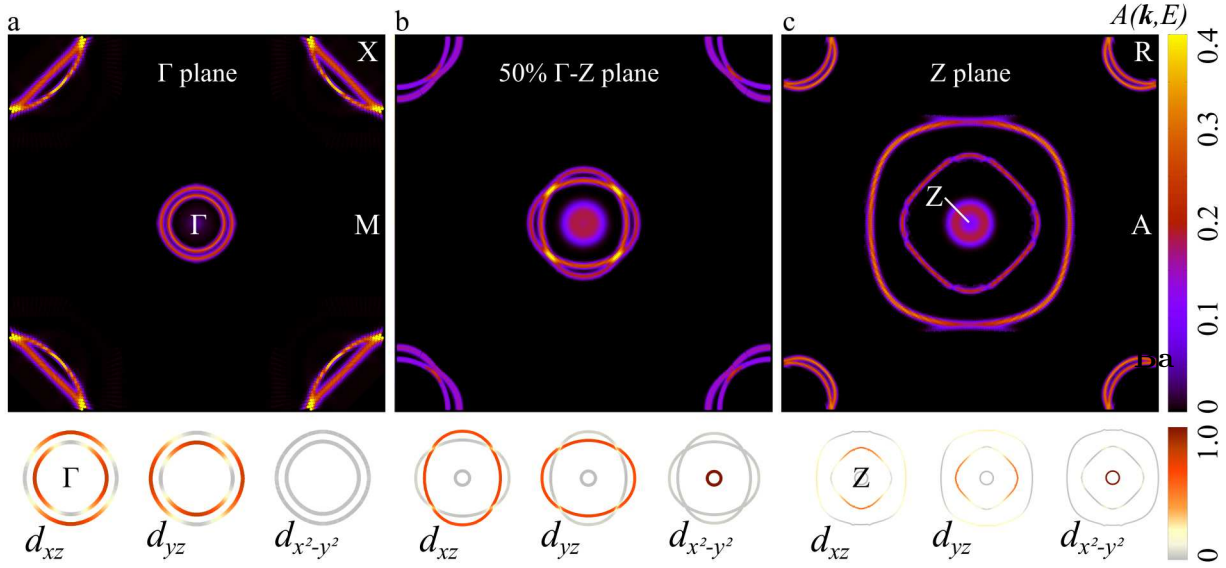

Figure 2.7: The 2D Fermi surfaces derived from the spectral function $A(\boldsymbol{k}, E_F)$ for (a) the $\boldsymbol{\Gamma}$-plane, (b) the basal plane positioned midway along the $\boldsymbol{\Gamma}$-$\boldsymbol{Z}$ direction, and (c) at the $\boldsymbol{Z}$-plane. In each of these cases the lower part of the respective panel shows the orbital character from the 2D effective Fermi surfaces, respectively.[20]

To interpolate the Fermi vectors we took advantage of the radial symmetric structure of the 2D effective Fermi surfaces to separate the different resulting partial surfaces. The cylindrical like shape surface in the middle was centred around the $\boldsymbol{\Gamma}$ and $\boldsymbol{Z}$ line, with 3 separated partial surfaces at the top and 2 at the $\boldsymbol{\Gamma}$-plane (Fig. 2.7 panel a and c). We went through every 2D effective Fermi surface and calculated the radius for all Fermi vectors in the plane. The radius was a perfect indicator to separate the different sheets from each other. Although there are some cases where two distinct sheets coming in contact, as it is the case in Figure 2.7 b) for the 4 contact points of the outer 2 partial surface. This can be identified with band degeneracy and crossing points between different bands. Below the spectral Fermi surface we depicted the 2D effective Fermi surface with colour gradient of the orbital characters $\boldsymbol{d}_{xz}$,$\boldsymbol{d}_{yz}$ and $\boldsymbol{d}_{x^2-y^2}$ (Fig. 2.7). With the sharply defined orbital characters Oc_n^{θ} it was possible to identify sheets coming in contact and separate them. In Figure 2.8 b) we plotted the filtered and linear interpolated Fermi vectors for the outer cylindrical like shaped surface and with colour-gradient for the $\tilde{\boldsymbol{dyz}}$ orbital. This was done for all 3 partial surfaces in the centre with dominant orbitals $\boldsymbol{d}_{xz}$,$\boldsymbol{d}_{yz}$ and $\boldsymbol{d}_{x^2-y^2}$, respectively. For the two partial surfaces on the edge, the contribution of the orbitals was not as strictly separated as it was for the centre ones, but they differ enough to distinguish the sheets. We projected each Fermi vector with angle and height on a 2-dimensional plane and used the bilinear interpolation to get a dense surface with all quantities like Bloch character, orbital character and radius interpolated. This could be easily transformed back into 3 dimensional coordinates (k_x, k_y, k_z) in the Brillouin zone (Fig. 2.8 panel c).

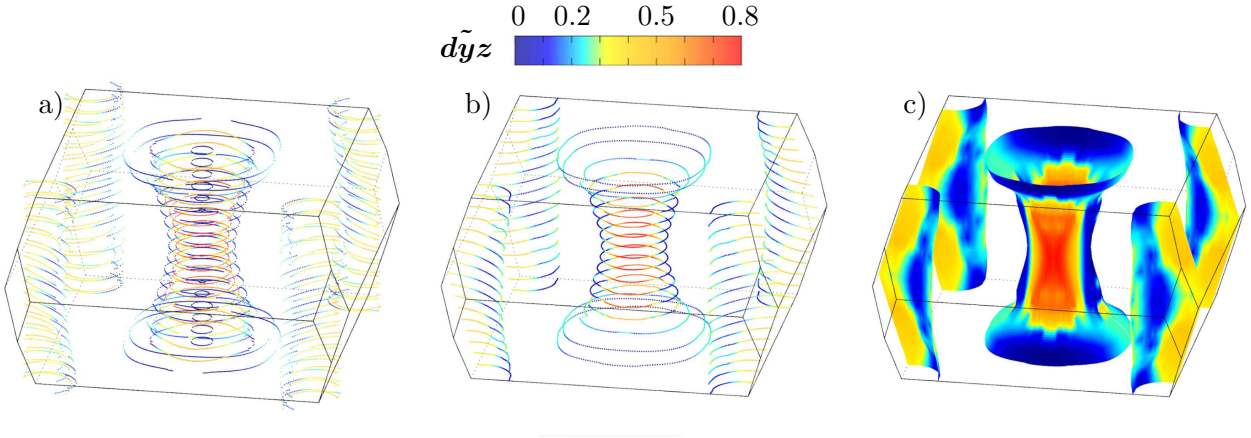

Figure 2.8: a) Shows the Fermi vectors from the unfolding calculations of $BaFe_{1.5}Ru_{0.5}As_2$ with a 8 times bigger super cell. The Fermi vectors were obtained with *bands4VASP*. b) Depicts the radial filtered and linear interpolated data with one centre at the line between $\boldsymbol{\Gamma}$ and $\boldsymbol{Z}$ and the other one between $\boldsymbol{X}$ and $\boldsymbol{R}$. The linear interpolation was done to get an equidistant pattern of Fermi vectors for a level, which simplifies the bilinear interpolation later on. c) The bilinear interpolated 3D Fermi surface obtained from the effective band structure for the orbital character $\boldsymbol{\tilde{dyz}}$

Finally we merged all the calculated surfaces in the first Brillouin zone. The results are shown in Figure 2.9, where we put all significant information and results of the project and testcase $BaFe_{1.5}Ru_{0.5}As_2$ together. Starting with the shape of the effective Fermi surface and comparing it with the 3D-FS of $BaFe_2As_2$ and $BaRu_2As_2$, one can see clearly the invariance, according the Ru concentration, of the partial surfaces at the edges of the Brillouin zone which are associated as electron pockets. However the cylindrical like shaped surfaces around the centre of BZ forming hole pockets change there size and shape drastically with the Ru concentration. The outer two partial surfaces share the orbitals $\boldsymbol{d}_{xz}$ and $\boldsymbol{d}_{yz}$ (Fig. 2.9 panel b), whereas the inner one is dominated by the $\boldsymbol{d}_{x^2-y^2}$ orbital (Fig. 2.9 panel c). The undoped $BaFe_2As_2$ has three almost cylindrical shaped surfaces in k_z direction. The 25% Ru-doped $BaFe_{1.5}Ru_{0.5}As_2$ shows more conical shaped surfaces at the centre. At the basal plane around $\boldsymbol{\Gamma}$ the hole pockets are getting smaller with an increasing Ru concentration as it is shown in Figure 2.6 iii) and the third most inner partial surface ($\boldsymbol{d}_{x^2-y^2}$ orbital character) vanished, whereas the diameters of the cylindrical like shapes at the $\boldsymbol{Z}$-plane are enlarged. For the 100% Ru-doped pnictide the hole pockets vanished completely at $\boldsymbol{\Gamma}$ as well as the third most inner partial surface, whereas the other two are extremely conic (Fig. 2.6 iii). We now want to put these geometrically and topology studies in context with results from superconducting measurements. Superconductivity emerges for the pnictide at a Ru concentration of $0.15 \leq x < 0.5$ with the highest critical temperature $T_c \backsimeq 20K$ at a Ru concentration of $x = 0.35$ [33]. There was also an experiment with $x = 0.36$ and no external magnetic field, in which they measured a critical temperature of $T_c = 20.2K$ [34], which seems to be the extremal point with the highest critical temperature. In our testcase $x = 0.25$ which is already in the superconducting phase, the $\boldsymbol{d}_{x^2-y^2}$

dominant partial surface vanished at basal $\boldsymbol{\Gamma}$-plane but is still present at the $\boldsymbol{Z}$-plane (Fig. 2.7 i and iii). At the estimated limit case $x = 0.5$ the two hole pockets around $\boldsymbol{\Gamma}$ with $\boldsymbol{d}_{xz}$ and $\boldsymbol{d}_{yz}$ orbital character are fused together (see figure 2.6), which could be an indicator for the collapse of the superconducting state. At this point we want to remark that the experimental results found with ARPES measurements [35]-[36] deviates from the behaviour of the $\boldsymbol{d}_{x^2-y^2}$ orbital. Where the experimental data show only a marginal influence of the Ru substitution on the $\boldsymbol{d}_{x^2-y^2}$ orbital in our simulations based on DFT calculations [28].

The effective Fermi surface in the results (Fig. 2.9 panel a) shows the distribution of the Bloch character. It is mostly equally distributed, despite some brighter spots which represents lower Bloch character values. There are two reasons for that:

- The inner $\boldsymbol{d}_{x^2-y^2}$ dominant partial surface has a slightly lower value for the Bloch character $\boldsymbol{P}_{\boldsymbol{K}m}(\boldsymbol{k}_i)$, which means that the projections of super cell eigenstates $|\boldsymbol{K}m\rangle$ on the primitive cell eigenstates $|\boldsymbol{k}n\rangle$ are weaker. This fits with the considerations before, where an increase of the Ru concentration shrinks and finally vanishes the inner partial surface in DFT simulations.

- For this representation we summed the Bloch character for all locally close enough eigenstates. There are some spots where the sheets are in contact with each other, which are degenerated eigenstates. These eigenstates share the same Bloch character, but during the process of separating them the Bloch character was split into two.

In the right inset in Figure 2.9 a) we demonstrated the difference of radial and orthogonal contributed $\boldsymbol{k}$-point sampling, which shows clearly that a non-matching geometry in the $\boldsymbol{k}$-point sampling cases an irregular distribution of the resulting Fermi vectors. That can lead to a distorted effective Fermi surface. The inset on the left side shows the eigenstates which were used for automated calculation of the Fermi vectors.

Ones the effective Fermi surface is determined the projection of the states on the orbitals as well the contribution of each element are determined too. In Figure 2.9 d) we depicted the contribution of the As atoms, caused by the hybridization with states from Fe atoms. This leads to more dominant states close to the $\boldsymbol{Z}$-plane and at the edges around $\boldsymbol{X}$.

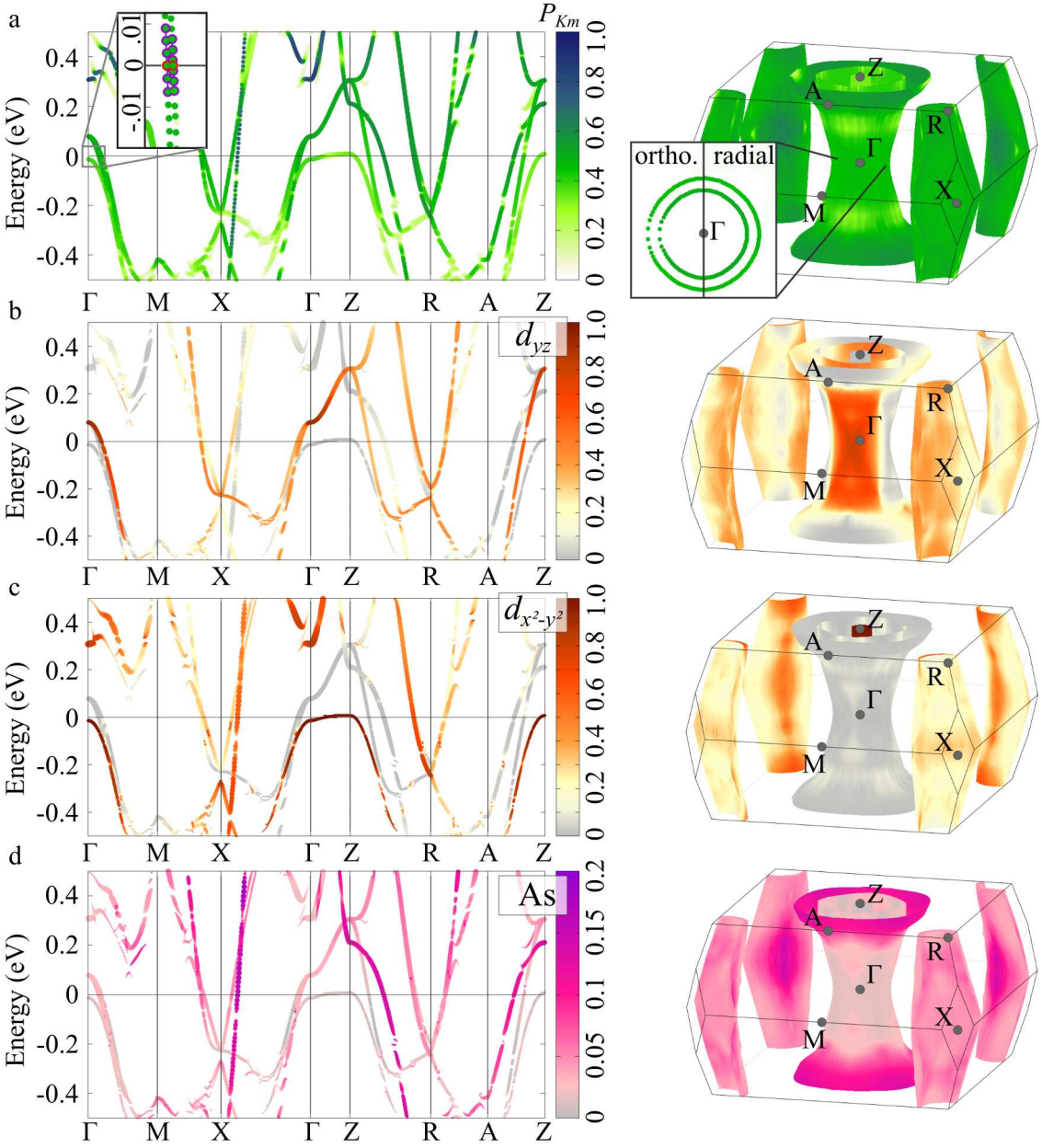

Figure 2.9: Summary of the results from unfolding with the testcase $BaFe_{1.5}Ru_{0.5}As_2$. Panel (a) shows the effective band structure and 3D effective Fermi surface with a colour gradient indicating $\boldsymbol{P}_{\boldsymbol{K}m}$. The insets show the Fermi wave vector identification with bands4VASP and the centre of a 2D effective Fermi surface with orthogonal (left) and radial (right) $\boldsymbol{k}$-point sampling in the Brillouin zone. Panel (b–d) depicting the effective band structure with colour gradient representing (b) $\boldsymbol{d}_{yz}$ and (c) $\boldsymbol{d}_{x^2-y^2}$ orbital character of Fe atoms and (d) the overall contribution from As atoms. The 3D effective Fermi surfaces with the respective colour gradient are shown on the right side [20].

Chapter 3

Conclusions

The numerical implementation of the eigenstate unfolding scheme in VASP and the post-processing tool bands4VASP are powerful tools which facilitate the analysis of the characteristics of materials, especially conducting properties. Obviously the advantage lies in investigating materials with disorders, vacancies, impurities or doped materials, which need a large super cell for an accurate description. Other situations that require large supercells are also suitable, such as the $TiO_2(110)$ analysis which needed a large surface area. In the benchmark section we tested the improved unfolding implementation in VASP and even with the 16 times larger super cell (80 atoms) and 300 $\boldsymbol{k}$-points for one line calculation, we didn't reached the memory limit on the "nowadays obsolete" VSC-3 high-performance computing facilities, proving the efficiency of our implementation. The super cell of the pristine rutile $TiO_2(110)$ contained even 363 atoms. This enables the calculation of effective band structure and effective Fermi surfaces for doping ratios which need huge super cells. For example the Ru concentration of $x = 0.36$, which were used in superconducting measurements [33], needs at least a super cell of 125 atoms ($Ba_{25}Fe_{32}Ru_{18}As_{50}$) to be represented. The procedures introduced in this work are capable of calculating EBS and the effective Fermi surface of this compound. This could help to understand the correlation of isovalent doping with the phenomena of superconduction. Nowadays fermiology is getting more attention, because it gets easier to compute complex hypersurfaces with rapidly increasing computational power. The connection of the shape and topology from a Fermi surface to conducting behaviour is still studied and explored. The effective Fermi surface, which we derived from the effective band structure is an useful supplementation to Fermi surfaces for the analysis of doping, impurities and other structural defects. As Kaganov and Lifshitz wrote ones down, the Fermi surface is "*the stage on which the drama of the life of the electron is played out*" [37] and the drama of the electron is too thrilling to miss it.

Appendix A

Fermi Surface: A Quantitative description

To understand the correlation of Fermi surface with the composition and structure of a crystal, it is descriptive to start with the dispersion relation of a free electron $E(\boldsymbol{k}) = \frac{\hbar^2}{2m}\boldsymbol{k}^2$. In a 3-dimensional $\boldsymbol{k}$-space, the surface of constant energy $E(\boldsymbol{k}) = E_F$ forms a sphere, the so called Fermi sphere with radius $k_F = (3\pi^2 n)^{\frac{1}{3}}$, where n is the number of electrons per atom site. For a better clarity we are going to consider a simple quadratic lattice, which results in a 2-dimensional quadratic Brillouin zone in $\boldsymbol{k}$-space $(\boldsymbol{k}_x, \boldsymbol{k}_y)$, where the dispersion relation $E(\boldsymbol{k})$ of the free electron is a paraboloid with an upper limit at $E(\boldsymbol{k}) = E_F$. Projected on a 2-dimensional plane, we get a circular Fermi surface with radius $k_F = (3\pi^2 n)^{\frac{1}{3}}$. In Figure A.1 there are 2 different Fermi surfaces A and B. The radius k_F of A is larger than the border of the Brillouin zone $k_F > \frac{\pi}{a}$, whereas the Fermi surface B is completely inside the first Brillouin zone. Physically speaking, Fermi surface A has a higher electron number per atom site and a higher total energy. It stands out, that even without a potential the size and shape of the Brillouin zone affects the appearance of the Fermi surface, which we will go into more detail later on.

If we now "switch on" the periodic potential, which we discussed in Section 1.2, the Fermi surface should feature some kind of perturbation. It will only be effected if it protrudes over the first Brillouin zone, which means that there are enough electrons per atom site to generate a large enough Fermi radius $k_F = (3\pi^2 n)^{\frac{1}{3}} \geq \frac{\pi}{a}$, otherwise it would stay a simple circle.

To get an analytic point of view we start with the Schrödinger equation in $\boldsymbol{k}$-space (Eq. 1.18) and the condition that there always exists a $\boldsymbol{G}$ which translates any arbitrary $\boldsymbol{k}'$ into the first Brillouin zone $\boldsymbol{k} = \boldsymbol{k}' + \boldsymbol{G}$, we can derive the following approximation for the coefficients of the potential (see [19] for the entire derivation):

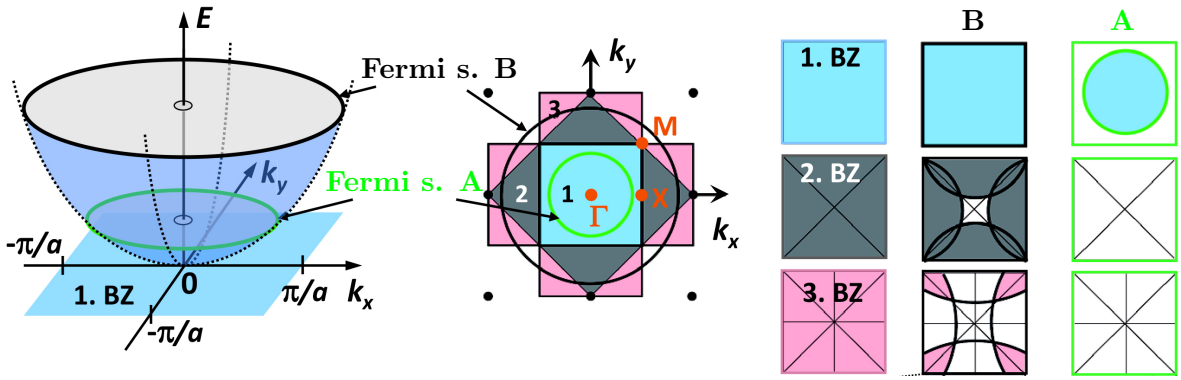

Figure A.1: On the left side the energy dispersion relation $E(\boldsymbol{k})$ of a free electron in a simple quadratic lattice is shown with two different exemplary Fermi surfaces A and B, where B has a larger number of electrons per atom site. In the middle are the first 3 Brillouin zones of a simple quadratic lattice in the extended zone scheme, with Fermi surface A inside the first Brillouin zone and Fermi surface B in the second and third Brillouin zone. On the right side are the first three Brillouin zones without a Fermi surface, for Fermi surface B and A, respectively. Adapted from [16].

$$C_{\boldsymbol{k}-\boldsymbol{g}} \simeq \frac{V_{-\boldsymbol{g}} C_{\boldsymbol{k}}}{\frac{\hbar^2}{2m}(k^2 - |\boldsymbol{k}-\boldsymbol{g}|^2)} \tag{A.1}$$

With the approximation that only the coefficients $C_{\boldsymbol{k}-\boldsymbol{g}}$ with large values have a significant contribution to the sum in Eq. 1.18, we get the condition:

$$k^2 \simeq |\boldsymbol{k}-\boldsymbol{g}|^2 \tag{A.2}$$

This condition is identical to the Laue-Bragg interference and is fulfilled for every wave vector from the centre to the border of a Brillouin-zone [19], which means that we get standing electron waves at the border of the Brillouin zone. Hence the perpendicular part of the electron waves group velocity $\nabla_k \frac{E}{\hbar}$ is zero and therefore the gradient of $E(\boldsymbol{k})$ is parallel to the border of the Brillouin zone. That leads to the conclusion, that lines of constant energy $E(\boldsymbol{k}) = const$ are perpendicular to the Brillouin zone borders. This deforms the Fermi surface and breaks the circular shape in our example, as shown in Figure A.2.

The same effect causes the energy gaps at the Brillouin zone borders of the band structure. The deformation of the Fermi surface near the zone borders, enlarges the volume of the second Brillouin zone in the same amount as it decreases the volume of the third BZ. This enables more electrons to be in the second BZ. Electrons in a lower Brillouin zone have lower energy, which lowers the total energy of the system. This is indeed the case for a solid body, a system with a periodic potential.

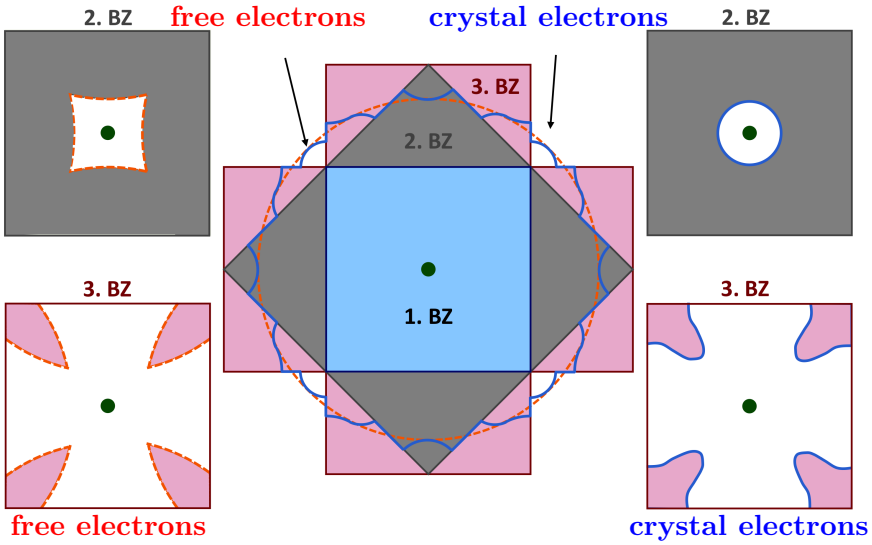

Figure A.2: Fermi surfaces of the first 3 Brillouin zones of free electrons (left) and crystal electrons (right) of a simple quadratic lattice. The extended zone scheme in the middle shows the Fermi surface of the free electron system (red dashed circle) and the Fermi surface of the crystal electrons (blue line). Adapted from [16].

Appendix B

List of input variables for bands4Vasp

- **EDIF** - Energy diffusion from the unfolding calculation. EDIF defines the maximal energy difference at one $\boldsymbol{k}$-point, in between this interval all energy states will be merged and represented in the processed data as one state.

- **EGAP** - defines the maximal energy difference of states from proximate $\boldsymbol{k}$-points. Eigenstates from proximate $\boldsymbol{k}$-points with an energy difference less than this value are considered to belong to the same band. This is used for the Fermi vector calculation.

- **BAVERAGE** - If BAVERAGE is set to .TRUE. the weighted average of the Bloch character is calculated and represented in the processed data, else the values will summed up.

- **OAVERAGE** - If OAVERAGE is set to .TRUE. the weighted average of the orbital character is calculated and represented in the processed data, else the values were summed up.

- **BLOCH_THRESHOLD** - sets the minimal Bloch character value. Energy states with a Bloch character less than BLOCH_THRESHOLD will rejected.

- **DBLOCH** - defines the maximal Bloch character difference for proximate energy states of the same $\boldsymbol{k}$-points to belong to the same band.

- **ODISTINCT** - defines the maximal orbital character difference for proximate energy states of each orbital to belong to the same band.

- **GRADIENTD** - multiplied with **EGAP** defines the energy interval around the estimated value for which the energy value at the proximate ***k***-point has to be in $E \in \{E_{prox} \pm EGAP \cdot GRADIENTD\}$.

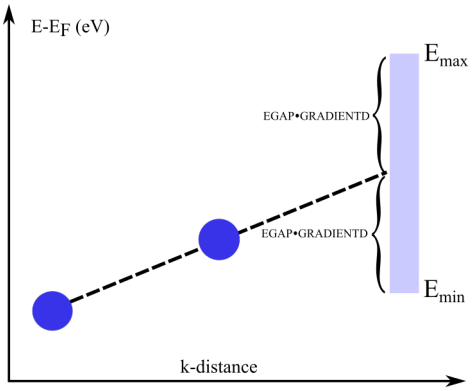

Figure B.1: Sketch for demonstrating the meaning of **GRADIENTD**

- **NPOINTS** - defines the number of energy states above and below the Fermi level, which will be included in the Fermi vector calculation.

- **BNDDIFF** - If BNDDIFF is set to .TRUE. (default) bands4VASP considers band crossing from bands with different band indices. If set to .FALSE., only bands with the same band index are considered as one band.

Appendix C

German Abstract

Moderne Rechenanlagen ermöglichen die Anwendung der Dichtefunktionaltheorie (DFT) zur Untersuchung komplexer physikalischer und chemischer Phänomene. In vielen Fällen erfordern diese Berechnungen die Verwendung großer Superzellen, um die gewünschten Eigenschaften genau darzustellen. Jedoch stellen Superzellen eine Herausforderung dar, da sie zu kleinen Brillouin-Zonen im reziproken Raum führen, was zu gefalteten elektronischen Eigenzuständen führt, die wiederum schwer zu analysieren und interpretieren sind. Um dieses Problem anzugehen, wurden verschiedene Techniken vorgeschlagen, um die elektronischen Bandstrukturen von Superzellen in den reziproken Raum einer idealen primitiven Zelle zu entfalten. In diesem Zusammenhang stellen wir eine Entfaltungsmethode vor, die direkt in das Vienna Ab initio Simulation Package (VASP) integriert ist. Dieser Ansatz ist weitaus sparsamer bezüglich der Rechenressourcen und bietet eine automatische Abbildung vom reziproken Raum der Superzelle auf die Brillouin-Zone der primitiven Zelle. Unser Algorithmus, gekoppelt mit einem integrierten Post-Processing-Tool namens bands4VASP, erleichtert die Berechnung von effektiven Bandstrukturen, Fermi-Flächen und Spektralfunktionen. Wir werden die Nützlichkeit dieser Methode demonstrieren, indem wir sie auf verschiedene komplexe Szenarien anwenden. Dies zeigen wir am Beispiel der Auswirkungen von Dotierung auf die Banddispersion des Supraleiters $BaFe_{2(1-x)}Ru_{2x}As_2$ und der Ableitung der effektiven 3D Fermi-Fläche.

Bibliography

[1] W. Kohn P. Hohenberg. "Inhomogeneous Electron Gas." In: *Physical Review* 136.3B (Nov. 1964). DOI: 10.1103/PhysRev.136.B864. URL: https://doi.org/10.1103/PhysRev.136.B864.

[2] Douglas Rayner Hartree. *The calculation of atomic structures*. English. 1957.

[3] R. Oppenheimer M. Born. *Annalen der Physik, Band 84: Zur Quantentheorie der Molekeln*. German. 1927.

[4] Lu Jeu Sham Walter Kohn. "Self-Consistent Equations Including Exchange and Correlation Effects." In: *Physical Review* 140.A4 (1965). DOI: 10.1103/PhysRev.140.A1133. URL: https://journals.aps.org/pr/abstract/10.1103/PhysRev.140.A1133.

[5] J. C. Slatter. In: *The Theory of Complex Spectra* 34.10 (June 1929). DOI: 10.1103/PhysRev.34.1293. URL: https://journals.aps.org/pr/abstract/10.1103/PhysRev.34.1293.

[6] Christian B. Lang and Norbert Pucker. *Mathematische Methoden in der Physik*. German. Springer Spektrum, 2016. ISBN: 978-3-662-49312-0. DOI: 10.1007/978-3-662-49313-7.

[7] Diola Bagayoko. "Understanding density functional theory (DFT) and completing it in practice." In: *AIP Advances* 4 (2014). DOI: 10.1063/1.4903408. URL: https://pubs.aip.org/aip/adv/article/4/12/127104/240423/Understanding-density-functional-theory-DFT-and.

[8] D. Bagayoko G. L. Zhao and T. D. Williams. "Local-density-approximation prediction of electronic properties of GaN, Si, C, and RuO2." In: *Physical Review B* 60 (1999). DOI: 10.1103/physrevb.60.1563. URL: https://journals.aps.org/prb/abstract/10.1103/PhysRevB.60.1563.

[9] J.A. Chevary J. P. Perdew, M. R. Pederson S. H. Vosko K. A. Jackson, and C. Fiolhais D. J. Singh. "Atoms, molecules, solids, and surfaces: Applications of the generalized gradient approximation for exchange and correlation." In: *Physical Review B* 46.11 (1992). DOI: https://doi.org/10.1103/PhysRevB.46.6671. URL: https://journals.aps.org/prb/abstract/10.1103/PhysRevB.46.6671.

[10] M. Ernzerhof J. P. Perdew K. Burke. "General Gradient Approximation Made Simple." In: *Physical Review Letters* 77.18 (1996). DOI: https://doi.org/10.1103/PhysRevLett.77.3865. URL: https://journals.aps.org/prl/abstract/10.1103/PhysRevLett.77.3865.

[11] Kieron Burke, John P. Perdew, and Yue Wang. "Derivation of a Generalized Gradient Approximation: The PW91 Density Functional." In: *Electronic Density Functional Theory: Recent Progress and New Directions*. Ed. by John F. Dobson, Giovanni Vignale, and Mukunda P. Das. Boston, MA: Springer US, 1998. ISBN: 978-1-4899-0316-7. DOI: 10.1007/978-1-4899-0316-7_7. URL: https://doi.org/10.1007/978-1-4899-0316-7_7.

[12] K. W. Jacobsen B. Hammer and J. K. Norskov. "Role of nonlocal exchange correlation in activated adsorption." In: *Physical Review Letters* 70 (1993). DOI: https://doi.org/10.1103/PhysRevLett.70.3971. URL: https://journals.aps.org/prl/abstract/10.1103/PhysRevLett.70.3971.

[13] A. D. Becke. "Density-functional thermochemistry. I. The effect of the exchange-only gradient correction." In: *The Journal of Chemical Physics* 96.3 (1992). DOI: https://doi.org/10.1063/1.462066. URL: https://pubs.aip.org/aip/jcp/article-abstract/96/3/2155/802867/Density-functional-thermochemistry-I-The-effect-of?redirectedFrom=fulltext.

[14] University of Vienna. *Vienna Ab-initio Simulation Package (VASP)*. https://www.vasp.at. 2023.

[15] University of Vienna. *Vienna Ab-initio Simulation Package (VASP) - GGA*. https://www.vasp.at/wiki/index.php/GGA. 2023.

[16] Dr. Achim Marx Prof. Dr. Rudolf Gross. *Festkörperphysik*. German. Oldenbourg Verlag Muenchen, 2012. ISBN: 978-3-486-71294-0.

[17] Prof. Dr. Siegfried Hunklinger. *Festkörperphysik*. German. De Gruyter, 2018. ISBN: 978-3-11-056774-8.

[18] Charles Kittel. *Introduction to Solid State Physics*. English. John Wiley and Sons, 1956. ISBN: 978-1-119-45416-8.

[19] N. W. Ashcroft and N. D. Mermin. *Festkörperphysik*. German. Springer, 2012. ISBN: 9783486713015.

[20] David Dirnberger et al. "Electronic State Unfolding for Plane Waves: Energy Bands, Fermi Surfaces, and Spectral Functions." In: *The Journal of Physical Chemistry C* 125.23 (2021). PMID: 34276866, pp. 12921–12928. DOI: 10.1021/acs.jpcc.1c02318. eprint: https://doi.org/10.1021/acs.jpcc.1c02318. URL: https://doi.org/10.1021/acs.jpcc.1c02318.

[21] Voicu Popescu and Alex Zunger. "Effective band structure of random alloys." In: *Physical Review Letters* 104.23 (June 2010), p. 236403. ISSN: 00319007. DOI: 10.1103/PhysRevLett.104.236403. URL: https://link.aps.org/doi/10.1103/PhysRevLett.104.236403.

[22] Voicu Popescu and Alex Zunger. "Extracting E versus k effective band structure from supercell calculations on alloys and impurities." In: *Physical Review B* 85.8 (Feb. 2012), p. 085201. ISSN: 1098-0121. DOI: 10.1103/PhysRevB.85.085201. URL: https://link.aps.org/doi/10.1103/PhysRevB.85.085201.

[23] Dirnberger, David and Kresse, Georg and Franchini, Cesare and Reticcioli, Michele. *bands4vasp post-processing package*. https://github.com/QuantumMaterialsModelling/bands4vasp. 2021.

[24] A. Thaler et al. "Physical and magnetic properties of Ba(Fe1-xRux) 2As2 single crystals." In: *Physical Review B - Condensed Matter and Materials Physics* 82.1 (July 2010), p. 014534. ISSN: 10980121. DOI: 10.1103/PhysRevB.82.014534. URL: http://link.aps.org/doi/10.1103/PhysRevB.82.014534%20https://%20link.aps.org/doi/10.1103/PhysRevB.82.014534.

[25] L. Liu et al. "In-plane electronic anisotropy in the antiferromagnetic orthorhombic phase of isovalent-substituted Ba(Fe1-xRux)2As2." In: *Physical Review B - Condensed Matter and Materials Physics* 92.9 (2015), p. 094503. ISSN: 1550235X. DOI: 10.1103/PhysRevB.92.094503. URL: http://link.aps.org/doi/10.1103/PhysRevB.92.094503.

[26] Limin Wang et al. "Effects of disordered Ru substitution in BaFe2As2: Possible realization of superdiffusion in real materials." In: *Physical Review Letters* 110.3 (Jan. 2013), p. 037001. ISSN: 00319007. DOI: 10.1103/PhysRevLett.110.037001. URL: https://link.aps.org/doi/10.1103/PhysRevLett.110.037001.

[27] M. Reticcioli et al. "Effective band structure of Ru-doped BaFe2As2." In: *Journal of Physics: Conference Series* 689.1 (2016). ISSN: 17426596. DOI: 10.1088/1742-6596/689/1/012027.

[28] M. Reticcioli et al. "Ru doping in iron-based pnictides: The "unfolded" dominant role of structural effects for superconductivity." In: *Physical Review B* 95.21 (June 2017), p. 214510. ISSN: 24699969. DOI: 10.1103/PhysRevB.95.214510. URL: http://arxiv.org/abs/1701.02498%20http://link.aps.org/doi/%2010.1103/PhysRevB.95.214510.

[29] Austrian initiative on high performance computing. *Vienna Scientific Cluster 3 (VSC3)*. https://vsc.ac.at/systems/vsc-3/. 2020.

[30] Michele Reticcioli et al. "Interplay between Adsorbates and Polarons: CO on Rutile TiO2 (110)." In: *Physical Review Letters* 122.1 (Jan. 2019), p. 016805. ISSN: 10797114. DOI: 10.1103/PhysRevLett.122.016805. URL: http://arxiv.org/abs/1807.05859%20http://dx.doi.org/10.1103/%20PhysRevLett.122.016805%20https://link.aps.org/doi/10.1103/%20PhysRevLett.122.016805.

[31] Matthew D. Watson et al. "Probing the reconstructed Fermi surface of antiferromagnetic BaFe2As2 in one domain." In: *npj Quantum Materials* 4.1 (July 2019), p. 36. ISSN: 2397-4648.

DOI: 10.1038/s41535-019-0174-z. URL: https://www.nature.com/articles/s41535-019-0174-z.

[32] Lijun Zhang and D. J. Singh. "Electronic structure of Ba(Fe, Ru) 2 As 2 and Sr(Fe, Ir) 2 As 2 alloys." In: *Physical Review B* 79 (2009). DOI: 10.1103/PhysRevB.79.174530. URL: https://journals.aps.org/prb/abstract/10.1103/PhysRevB.79.174530.

[33] F. Rullier-Albenque et al. "Hole and electron contributions to the transport properties of $Ba(Fe_{1-x}Ru_x)_2As_2$ single crystals." In: *Phys. Rev. B* 81 (22 June 2010), p. 224503. DOI: 10.1103/PhysRevB.81.224503. URL: https://link.aps.org/doi/10.1103/PhysRevB.81.224503.

[34] Xuepeng Qiu et al. "Nodal superconductivity in Ba(Fe$_{1-x}$Ru$_x$)$_2$As$_2$ induced by isovalent Ru substitution." In: *arXiv: Superconductivity* (2011). URL: https://api.semanticscholar.org/CorpusID:117222572.

[35] N. Xu et al. "Effects of Ru substitution on electron correlations and Fermi-surface dimensionality in $Ba(Fe_{1-x}Ru_x)_2As_2$." In: *Phys. Rev. B* 86 (6 Aug. 2012), p. 064505. DOI: 10.1103/PhysRevB.86.064505. URL: https://link.aps.org/doi/10.1103/PhysRevB.86.064505.

[36] V. Brouet et al. "Impact of the two Fe unit cell on the electronic structure measured by ARPES in iron pnictides." In: *Phys. Rev. B* 86 (7 Aug. 2012), p. 075123. DOI: 10.1103/PhysRevB.86.075123. URL: https://link.aps.org/doi/10.1103/PhysRevB.86.075123.

[37] M. I. Kaganov and I. M. Lifshits. "Electron theory of metals and geometry." In: *Uspekhi Fizicheskikh Nauk* 129 (1979). DOI: 10.1070/PU1979v022n11ABEH005648. URL: https://www.physics.rutgers.edu/grad/601/CM601/koganovlifshitz.pdf.

[38] Kieron Burke. "Perspective on density functional theory." In: *The Journal of Chemical Physics* 136 (Apr. 2012). DOI: 10.1063/1.4704546. URL: http://dx.doi.org/10.1063/1.4704546.

[39] Gerd Cycholl. *Theoretische Festkörperphysik Band 1*. German. Springer, 2016. ISBN: 978-3-662-47140-1.

[40] N. Shanthi and D. D. Sarma. "Electronic structure of electron doped $SrTiO_3$: $SrTiO_{3-\delta}$ and $Sr_{1-x}La_xTiO_3$." In: *Physical Review B* 57.4 (Jan. 1998), pp. 2153–2158. ISSN: 0163-1829. DOI: 10.1103/PhysRevB.57.2153. URL: https://link.aps.org/doi/10.1103/PhysRevB.57.2153.

[41] N. D. M. Hine et al. "Supercell size scaling of density functional theory formation energies of charged defects." In: *Physical Review B* 79.2 (Jan. 2009), p. 024112. ISSN: 1098-0121. DOI: 10.1103/PhysRevB.79.024112. URL: https://link.aps.org/doi/10.1103/PhysRevB.79.024112.

[42] Wei Ku, Tom Berlijn, and Chi Cheng Lee. "Unfolding first-principles band structures." In: *Physical Review Letters* 104.21 (May 2010), p. 216401. ISSN: 00319007. DOI: 10.1103/PhysRevLett.104.216401. URL: https://link.aps.org/doi/10.1103/PhysRevLett.104.216401.

[43] Ryan P. Day et al. "Computational framework chinook for angle-resolved photoemission spectroscopy." In: *npj Quantum Materials* 4.1 (Dec. 2019), p. 54. ISSN: 23974648. DOI: 10.1038/s41535-019-0194-8. URL: http://arxiv.org/abs/1909.12081%20http://www.nature.com/%20articles/s41535-019-0194-8.

[44] H.J.W.M. Hoekstra et al. "Matrix elements in appearance potential spectroscopy of Al and its alloys." In: *Journal of Electron Spectroscopy and Related Phenomena* 42.1 (Jan. 1987), pp. 27–38. ISSN: 03682048. DOI: 10.1016/0368-2048(87)85003-X. URL: https://linkinghub.elsevier.com/retrieve/pii/036820488785003X.

[45] Timothy B. Boykin et al. "Approximate bandstructures of semiconductor alloys from tight-binding supercell calculations." In: *Journal of Physics Condensed Matter* 19.3 (Jan. 2007), p. 036203. ISSN: 09538984. DOI: 10.1088/0953-8984/19/3/036203. URL: http://stacks.iop.org/0953-8984/19/i=3/a=036203?%20key=crossref.e6e99b1c6cb7423678ca74007171d5ba.

[46] Timothy B. Boykin, Neerav Kharche, and Gerhard Klimeck. "Brillouin-zone unfolding of perfect supercells having nonequivalent primitive cells illustrated with a Si/Ge tight-binding parameterization." In: *Physical Review B - Condensed Matter and Materials Physics* 76.3 (July 2007), p. 035310. ISSN: 1550235X. DOI: 10.1103/PhysRevB.76.035310. URL: https://link.aps.org/doi/10.1103/PhysRevB.76.035310.

[47] J. Voit et al. "Electronic structure of solids with competing periodic potentials." In: *Science* 290.5491 (Oct. 2000), pp. 501–503. ISSN: 00368075. DOI: 10.1126/science.290.5491.501. URL: http://www.sciencemag.org/cgi/doi/10.1126/science.290.5491.501.

[48] C. Eckhardt, K. Hummer, and G. Kresse. "Indirect-to-direct gap transition in strained and unstrained SnxGe1-x alloys." In: *Physical Review B - Condensed Matter and Materials Physics* 89.16 (Apr. 2014), p. 165201. ISSN: 1550235X. DOI: 10.1103/PhysRevB.89.165201. URL: https://link.aps.org/doi/10.1103/PhysRevB.89.165201.

[49] Fawei Zheng, Ping Zhang, and Wenhui Duan. "Quantum Unfolding: A program for unfolding electronic energy bands of materials." In: *Computer Physics Communications* 189 (2015), pp. 213–219. ISSN: 00104655. DOI: 10.1016/j.cpc.2014.12.009. URL: http://dx.doi.org/10.1016/j.cpc.2014.12.009.

[50] Paulo V.C. Medeiros, Sven Stafström, and Jonas Björk. "Effects of extrinsic and intrinsic perturbations on the electronic structure of graphene: Retaining an effective primitive cell band structure by band unfolding." In: *Physical Review B - Condensed Matter and Materials*

Physics 89.4 (Jan. 2014), p. 041407. ISSN: 10980121. DOI: 10.1103/PhysRevB.89.041407. URL: https://link.aps.org/doi/10.1103/PhysRevB.89.041407.

[51] Paulo V.C. Medeiros et al. "Unfolding spinor wave functions and expectation values of general operators: Introducing the unfolding-density operator." In: *Physical Review B - Condensed Matter and Materials Physics* 91.4 (Jan. 2015), p. 041116. ISSN: 1550235X. DOI: 10.1103/PhysRevB.91.041116. URL: https://link.aps.org/doi/10.1103/PhysRevB.91.041116.

[52] Uthpala Herath et al. "PyProcar: A Python library for electronic structure pre/post-processing." In: *Computer Physics Communications* 251 (June 2020). ISSN: 00104655. DOI: 10.1016/j.cpc.2019.107080. URL: http://arxiv.org/abs/1906.11387.

[53] Vei Wang et al. "VASPKIT: A User-friendly Interface Facilitating High-throughput Computing and Analysis Using VASP Code." In: *arXiv* (Aug. 2019), pp. 1–26. URL: http://arxiv.org/abs/1908.08269.

[54] Peitao Liu et al. "Electron and hole doping in the relativistic Mott insulator Sr 2 IrO 4: A first-principles study using band unfolding technique." In: *Physical Review B* 94.19 (Nov. 2016), p. 195145. ISSN: 24699969. DOI: 10.1103/PhysRevB.94.195145. URL: http://link.aps.org/doi/10.1103/PhysRevB.94.195145.

[55] V. Brouet et al. "Significant Reduction of Electronic Correlations upon Isovalent Ru Substitution of $BaFe_2As_2$." In: *Phys. Rev. Lett.* 105 (8 Aug. 2010), p. 087001. DOI: 10.1103/PhysRevLett.105.087001. URL: https://link.aps.org/doi/10.1103/PhysRevLett.105.087001.

[56] Shilpam Sharma et al. "Superconductivity in Ru-substituted polycrystalline BaFe2-x Rux As2." In: *Physical Review B - Condensed Matter and Materials Physics* 81.17 (May 2010), p. 174512. ISSN: 10980121. DOI: 10.1103/PhysRevB.81.174512. URL: https://link.aps.org/doi/10.1103/PhysRevB.81.174512.

[57] M. J. Eom et al. "Evolution of transport properties of BaFe 2-xRu xAs 2 in a wide range of isovalent Ru substitution." In: *Physical Review B - Condensed Matter and Materials Physics* 85.2 (Jan. 2012), p. 024536. ISSN: 10980121. DOI: 10.1103/PhysRevB.85.024536. URL: https://link.aps.org/doi/10.1103/PhysRevB.85.024536.

[58] M. G. Kim et al. "Spin polarization of Ru in superconducting Ba(Fe0.795Ru 0.205)2As2 studied by x-ray resonant magnetic scattering." In: *Physical Review B - Condensed Matter and Materials Physics* 88.1 (July 2013), p. 014424. ISSN: 10980121. DOI: 10.1103/PhysRevB.88.014424. URL: http://link.aps.org/doi/10.1103/PhysRevB.88.014424.

[59] Shilpam Sharma et al. "Structural investigations in BaFe2 - X Rux As2 as a function of Ru and temperature." In: *Acta Crystallographica Section B: Structural Science, Crystal Engineering and Materials* 71.1 (2015), pp. 61–67. ISSN: 20525206. DOI: 10.1107/S2052520614023634. URL: http://arxiv.org/abs/1312.7055.

[60] T. R. Devidas et al. “Unification of the pressure and composition dependence of superconductivity in Ru substituted BaFe2As2.” In: *Solid State Communications* 185 (May 2014), pp. 62–66. ISSN: 00381098. DOI: 10.1016/j.ssc.2014.02.002. URL: http://linkinghub.elsevier.com/retrieve/pii/%20S0038109814000611.

[61] Smritijit Sen et al. “Origin of structural and magnetic transitions in BaFe2-xRuxAs2 materials.” In: *Superconductor Science and Technology* 27.12 (Dec. 2014), p. 122003. ISSN: 13616668. DOI: 10.1088/0953-2048/27/12/122003. URL: http://stacks.iop.org/0953-2048/27/i=12/a=122003?%20key=crossref.1d7b2c4fba7c253b8ea2b6eab5ec228b%20http://%20arxiv.org/abs/1408.3239.

[62] Wahyu Setyawan and Stefano Curtarolo. “High-throughput electronic band structure calculations: Challenges and tools.” In: *Computational Materials Science* 49.2 (2010), pp. 299–312. ISSN: 09270256. DOI: 10.1016/j.commatsci.2010.05.010. URL: http://dx.doi.org/10.1016/j.commatsci.2010.05.010.

[63] David S. Sholl and Janice A. Steckel. “DFT Calculations for Surfaces of Solids.” In: *Density Functional Theory*. Hoboken, NJ, USA: John Wiley and Sons, Inc., 2009, pp. 83–112. DOI: 10.1002/9780470447710.ch4. URL: http://doi.wiley.com/10.1002/9780470447710.ch4.

[64] Martin Setvin et al. “Direct view at excess electrons in TiO2 rutile and anatase.” In: *Physical Review Letters* 113.8 (Aug. 2014), p. 086402. ISSN: 10797114. DOI: 10.1103/PhysRevLett.113.086402. URL: https://link.aps.org/doi/10.1103/PhysRevLett.113.086402.

[65] Roger Rousseau, Vassiliki Alexandra Glezakou, and Annabella Selloni. “Theoretical insights into the surface physics and chemistry of redox-active oxides.” In: *Nature Reviews Materials* 5.6 (May 2020), pp. 460–475. ISSN: 20588437. DOI: 10.1038/s41578-020-0198-9. URL: http://dx.doi.org/10.1038/s41578-020-0198-9%20http://%20www.nature.com/articles/s41578-020-0198-9.

[66] Michele Reticcioli et al. “Formation and dynamics of small polarons on the rutile TiO2 (110) surface.” In: *Physical Review B* 98.4 (July 2018), p. 045306. ISSN: 24699969. DOI: 10.1103/PhysRevB.98.045306. URL: https://link.aps.org/doi/10.1103/PhysRevB.98.045306%20http://%20arxiv.org/abs/1805.01849.

[67] Michele Reticcioli et al. “Competing states on polar surfaces.” In: *under review* (2021).

[68] J. Z. Ma et al. “Spin fluctuation induced Weyl semimetal state in the paramagnetic phase of EuCd2As2.” In: *Science Advances* 5.7 (July 2019), eaaw4718. ISSN: 23752548. DOI: 10.1126/sciadv.aaw4718. URL: https://advances.sciencemag.org/content/5/7/eaaw4718.

[69] A. F. Santander-Syro et al. “Orbital symmetry reconstruction and strong mass renormalization in the two-dimensional electron gas at the surface of KTaO 3.” In: *Physical Review B - Condensed Matter and Materials Physics* 86.12 (Sept. 2012), p. 121107. ISSN: 10980121. DOI:

10.1103/PhysRevB.86.121107. URL: https://link.aps.org/doi/10.1103/PhysRevB.86.121107.

[70] Yahui Mao et al. "Interfacial Polarons in van der Waals Heterojunction of Monolayer SnSe 2 on SrTiO 3 (001)." In: *Nano Letters* 20.11 (Nov. 2020), pp. 8067–8073. ISSN: 1530-6984. DOI: 10.1021/acs.nanolett.0c02741. URL: https://pubs.acs.org/doi/10.1021/acs.nanolett.0c02741.